PONTIFICIA UNIVERSIDAD CATÓLICA DEL PERÚ

ESCUELA DE POSGRADO

Física de neutrinos de fuentes astronómicas y terrestres

Articulos presentados para optar el Título de Magister en Física que presenta:

Carlos Alberto Argüelles Delgado

Autores:

Carlos A. Argüelles Delgado, Mauricio Bustamante Ramírez, Alberto M. Gago Medina, Joachim Kopp

Asesor:

Dr. Alberto M. Gago Medina

Jurado:

Dr. Francisco A. De Zela Martinez
Dr. Hernán A. Castillo Egoavil

Lima, Julio 2012

Física de neutrinos de fuentes astronómicas y terrestres

Carlos Alberto Argüelles Delgado

Propuesto para el Grado de Magíster en Física
2012

Resumen

El presente es el resultado de las investigaciones realizadas durante la maestría en física bajo la supervisión de Alberto Gago. Se discutirán brevemente tres trabajos realizados en este periodo con el fin de obtener el grado de Magíster en Física.

Durante la última década y media numerosos experimentos han demostrado que los neutrinos se transforman entre sus diferentes sabores al propagarse. Las evidencias de este fenómeno, denominado oscilaciones de neutrinos por su carácter periódico, favorecen la hipótesis de que los neutrinos tienen masa y que los estados de masa y de sabor están relacionados por una matriz no diagonal. Las oscilaciones de neutrinos están caracterizadas por dicha matriz de mezcla y por las diferencias de masas cuadradas entre los diferentes estados de masa. Las entradas de dicha matriz de mezcla, llamada matriz Pontecorvo-Maki-Nakagawa-Sakata (PMNS), han sido medidas con creciente precisión por los experimentos de oscilación de neutrinos solares, atmosféricos, de reactores y de aceleradores. Recientemente se ha logrado medir todos los ángulos de mezcla involucrados en la rotación de los estados de masa, abriendo la posibilidad de observar una fase de violación de CP diferente de cero. Además, se ha establecido que hay, al menos, dos diferencias de masa cuadradas una correspondiente a la escala de oscilación solar y la otra a la atmosférica. Se sabe el orden entre los estados de masas que participan en la oscilación solar, pero no en el caso de la atmosférica. Futuros experimentos pretenden medir con mayor precisión la matriz de mezcla, determinar la jerarquía entre los estados de masa de neutrinos, la existencia de una fase CP y probar o negar la existencia de más estados de masa.

La reciente construcción del telescopio de neutrinos IceCube en el polo sur ha impulsado la búsqueda de física nueva en las fuentes astrofísicas vía el flujo de neutrinos de ultra alta energía. Para ello es importante tener un buen conocimiento del flujo esperado, sobretodo, a altas energías, donde existen menos datos. Entre las fuentes de neutrinos de ultra alta energía más importantes se encuentran los núcleos activos de galaxias (NAG). En este contexto, estudiamos el flujo difuso de neutrinos

predicho por dos modelos de producción de neutrinos en NAG. Estos modelos asumen como válida la correlación entre las NAG y la dirección de los rayos cósmicos de ultra alta energía hallada por el observatorio Pierre Auger (OPA) en Argentina. Tal que los datos obtenidos sobre los flujos de rayos cósmicos de alta energía en OPA pueden ser usados para estimar los flujos de neutrinos medidos acá en la tierra. No obstante, la relación entre estos dos flujos no es directa sino que en ella intervienen parámetros que dependen del modelo. En este estudio variamos los parámetros de los modelos y comparamos el número de eventos con los limites recientemente impuestos por IceCube. Encontramos que ambos modelos se encuentras desfavorecidos, por los limites actuales, y que en, caso de ser vistos, ellos podrían ser distinguidos con alta significancia.

Otra de las búsquedas realizadas por IceCube, en el régimen de los neutrinos de alta energía, son las señales de aniquilación de materia oscura provenientes del Sol. Una propuesta popular es considerar que la materia oscura es un WIMP (Weakly Interacting Massive Particle : Partículas Masivas de Interacción Débil). En este contexto la materia oscura puede ser caracterizada, en primera instancia, por su sección de choque y su masa. En los modelos donde el WIMP posee una sección de choque dependiente del spín (SD) la interacción de la materia oscura local con el Sol puede ser intensa. Esta interacción causaría una acumulación de materia oscura en el centro del Sol. La cual podría aniquilarse en partículas del modelo estándar las cuales, al decaer o interactuar con la materia solar, darían lugar a un flujo de neutrinos activos. Es la esperanza de experimentos como IceCube que dicho flujo de neutrinos sea observable. Hasta el momento no se ha observado dicho flujo, por lo que IceCube ha puesto limites en la sección de choque de la materia oscura. En este trabajo hacemos notar que dichos limites dependen de la forma de oscilación de los neutrinos; la cual conecta el flujo de neutrinos al salir del Sol con el detectado en la Tierra. En este trabajo consideramos modelos de neutrinos estériles. Estos suponen la existencia de sabores adicionales de neutrinos que no interactúan vía el boson Z, pero si se mezclan con los sabores activos afectando la probabilidad de oscilación. Encontramos que las modificaciones de los limites de materia oscura, en varios de estos modelos, son considerables debido a que aparecen nuevas resonancias, inducidas por la materia solar, que magnifican la transición entre neutrinos activos y estériles.

Como se ha hecho notar antes, la presencia de materia puede modificar sustancialmente la probabilidad de oscilación de los neutrinos. Usando esta propiedad planteamos un método para detectar regiones de densidad anómala en la corteza de la Tierra. Consideramos el caso en que los neutrinos provienen de un rayo-beta de

III

alta intensidad y un detector de carbono. Estudiamos la capacidad de esta configuración de descubrir cavidades con alto nivel de confianza. Además, en el caso de poder descubrirlas, estudiamos la capacidad que se tiene para medir sus parámetros, i.e. densidad, tamaño y posición. Para ello estudiamos numéricamente cuatro cavidades inspiradas en casos reales : una con una densidad similar al agua, otra de hierro, otra de metales pesados y otra con una densidad de electrones similar a la que, supuestamente, aparece antes de un sismo. Reconstruimos la cavidad en cada uno de los casos mencionados y analizamos la sensibilidad del método a la variación de los parámetros. Adicionalmente, explicamos el comportamiento de nuestros resultados teóricos con un modelo aproximado, llamado "slabs", en el que consideramos que la densidad es constante por tramos en vez de depender continuamente del radio de la Tierra. Finalmente dotamos de movilidad a nuestro detector y hacemos que nuestra fuente de neutrinos sea un haz orientable con el fin de mover el haz para hacer un barrido de toda la corteza terrestre. En este contexto definimos un parámetro que nos permitiría evaluar fácilmente y con alta confianza la presencia de la cavidad.
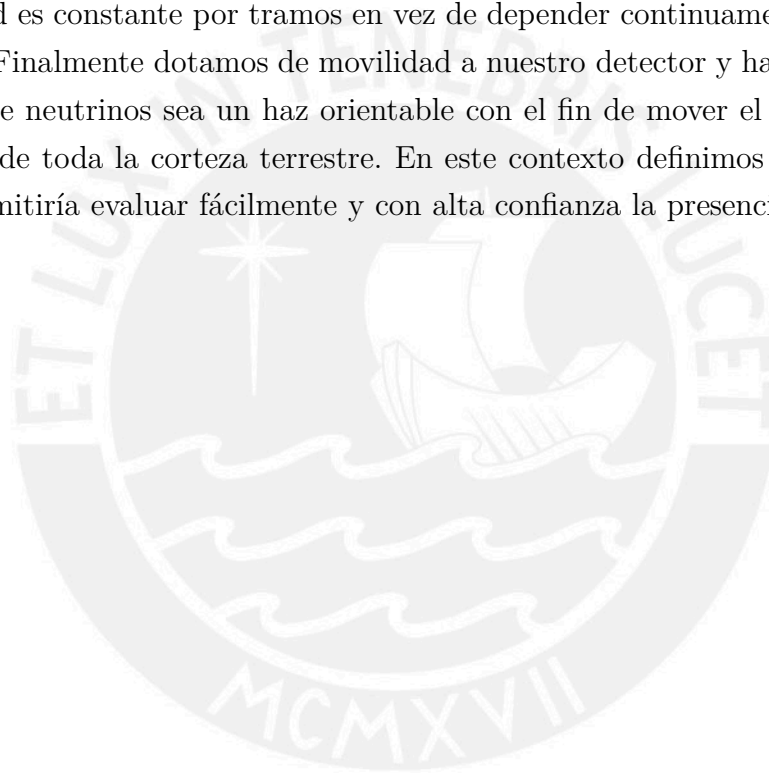
Agradecimientos

Agradezco a mis profesores de la maestría en física quienes, en estos años, me han proporcionado las herramientas para poder realizar este trabajo. En especial quisiera agradecer a los profesores Francisco de Zela, Eduardo Massoni, Hernán Castillo y Desiderio Vasquez por sus clases e instructivas discusiones. También quisiera agradecer a Myriam Pajuelo con quien siempre ha sabido alimentar mi entusiasmo por la astrofísica.

No puedo dejar de agradecer a mi asesor, el profesor Alberto Gago, quien no solo me ha enseñado cursos muy apasionantes y exigentes, sino que además a través de constantes discusiones y conversaciones ha dado forma a estos trabajos y a inculcado en mi una manera de hacer física. Estas discusiones han sido cuna de estos trabajos, es claro que sin su guia estos no hubieran podido llevarse acabo. Agradezco nuevamente a Alberto por el incansable entusiasmo y las constantes interrogantes. Es importante mencionar que estos trabajos no hubieran podido hacerse sin mis colegas Mauricio Bustamante y Joachim Kopp quienes no solo han aportado significativamente a estos trabajos, sino que además me han enseñado mucho. Gracias a ambos.

De igual manera no puedo obviar el apoyo de mi familia, en especial, el de mis padres, Carlos y Sarisa, quienes siempre han resaltado la importancia de la constancia y de seguir mis sueños. También debo resaltar el apoyo de mis hermanos Alonso y Sebastián, quienes, en estos años, han empezado exitosamente su vida académica. No veo manera en que estos trabajos se hubieran realizado sin su apoyo y constante aliento.

En estos años, como en mis estudios de pregrado, mis amigos y compañeros de la universidad siempre estaban dispuestos por discutir física con buen humor y camaradería. En especial le agradezco a Mauricio, Juan Pablo, Omar y Juan Carlos por las discusiones y tiempos divertidos. También quisiera agradecer por su genial compañía y charlas a Margot, Alvaro, Ana Paula, Ernesto, Majo, Kike, Rafaella, Christian y los demás estudiantes de física.

Durante estos estudios nuevos buenos amigos han aparecido y otros antiguos

han reaparecido. Son demasiados para listar, pero quisiera agradecer en especial a Alejandra, Mauricio, Yani, Oscar, Paco, Alvaro, Pancho y Cristina. Gracias a todos los amigos que han caminado a mi lado estos años.

Gracias a todos.

arXiv:1008.1396v2 [astro-ph.HE] 2 Dec 2010

IceCube expectations for two high-energy neutrino production models at active galactic nuclei

C.A. Argüelles,[a] **M. Bustamante,**[a,b] **and A.M. Gago**[a]

[a]Sección Física, Departamento de Ciencias, Pontificia Universidad Católica del Perú,
  Apartado 1761, Lima, Peru
[b]Theoretical Physics Department, Fermi National Accelerator Laboratory,
  P.O. Box 500, Batavia, IL 60510, USA

E-mail: c.arguelles@pucp.edu.pe, mbustamante@pucp.edu.pe, agago@pucp.edu.pe

Abstract. We have determined the currently allowed regions of the parameter spaces of two representative models of diffuse neutrino flux from active galactic nuclei (AGN): one by Koers & Tinyakov (KT) and another by Becker & Biermann (BB). Our observable has been the number of upgoing muon-neutrinos expected in the 86-string IceCube detector, after 5 years of exposure, in the range $10^5 \leq E_\nu/\text{GeV} \leq 10^8$. We have used the latest estimated discovery potential of the IceCube-86 array at the 5σ level to determine the lower boundary of the regions, while for the upper boundary we have used either the AMANDA upper bound on the neutrino flux or the more recent preliminary upper bound given by the half-completed IceCube-40 array (IC40). We have varied the spectral index of the proposed power-law fluxes, α, and two parameters of the BB model: the ratio between the boost factors of neutrinos and cosmic rays, $\Gamma_\nu/\Gamma_{\text{CR}}$, and the maximum redshift of the sources that contribute to the cosmic-ray flux, $z_{\text{CR}}^{\max}$. For the KT model, we have considered two scenarios: one in which the number density of AGN does not evolve with redshift and another in which it evolves strongly, following the star formation rate. Using the IC40 upper bound, we have found that the models are visible in IceCube-86 only inside very thin strips of parameter space and that both of them are discarded at the preferred value of $\alpha = 2.7$ obtained from fits to cosmic-ray data. Lower values of α, notably the values 2.0 and 2.3 proposed in the literature, fare better. In addition, we have analysed the capacity of IceCube-86 to discriminate between the models within the small regions of parameter space where both of them give testable predictions. Within these regions, discrimination at the 5σ level or more is guaranteed.

Contents

1   Introduction

Active Galactic Nuclei (AGN) are the most luminous persistent objects in the Universe, emitting radiation along almost the entire electromagnetic spectrum, with typical luminosities on the order of 10^{42} erg s^{-1} (see, e.g., [1, 2]). There is evidence that supports the idea that AGN are powered by matter accreting onto a central supermassive black hole, with a mass between 10^6 and 10^{10} times the solar mass [3, 4]. In some cases an enormous amount of energy is released in the form of two highly-collimated relativistic jets that emerge in opposite directions, perpendicularly to the accretion disc. Although the composition of these jets is unknown, it is widely believed that they contain high-energy charged particles, such as electrons, protons, and ionised nuclei, which have been accelerated as a result of the repeated crossings of the shock fronts that exist within gas clouds moving at relativistic speeds along the jets. Such a process would be able to give protons and nuclei energies of up to $\sim 10^{20}$ eV [5, 6].

Recently, the Pierre Auger Observatory (PAO) claimed to have detected 69 cosmic-ray events with energies above 55 EeV [7] (see also [8]), providing evidence of the anisotropy in the arrival directions of utrahigh-energy cosmic rays (UHECRs). Based on the observation of 29 of these events having an angular separation of less than 3.1° from the positions of AGN in the 12th edition Véron-Cetty & Véron catalogue [9], a possible correlation was found with AGN lying relatively close, at distances of 75 Mpc or less. Even though the claim on the correlation has lost some ground since the first publication of the Auger results [10, 11], it still constitutes a possible hint towards identifying AGN as the sources of the highest-energy cosmic rays. It is also believed that AGN could be sites of ultra-high-energy (UHE) neutrino production. These would be produced in the interactions of UHE charged particles among

themselves and with the ambient photons. Therefore, under the assumption that cosmic-ray emission is accompanied by neutrino emission [12–14], Auger's claim can be used to normalise the neutrino flux predicted by astrophysical models of AGN.

In the present work, we have focused on two such models of neutrino production that take into account Auger's results: one by H. B. J. Koers & P. Tinyakov [15] and another one by J. Becker & P. L. Biermann [16], which we will call hereafter the KT and BB models, respectively. They differ greatly in their assumptions and, within some regions of their parameter spaces, on their predictions of the neutrino fluxes. We have assessed the possibility of observing these two fluxes in the km-scale IceCube neutrino telescope at the South Pole, by allowing their respective model parameters to vary within given boundaries, and calculating the corresponding number of high-energy muon-neutrinos expected in the detector. In doing this, we have taken into account the experimental upper bound on the neutrino flux set by the AMANDA-II experiment [17], an upper bound set by IceCube [18] in its 40-string configuration, and the signal discovery potential of high-energy astrophysical neutrinos in the completed 86-string IceCube array. Furthermore, we have also explored the parameter space for regions where the event-number predictions from the two production models can be distinguished from each other.

The remaining of the paper is divided as follows. In Section 2, we describe the salient features of the KT and BB models, and show explicitly how the observations from the PAO enter the flux normalisation. Section 3 introduces current and envisioned experimental bounds on the high-energy extra-terrestrial neutrino flux. In Section 4 we allow the parameters in the KT and BB models to vary within given bounds, and calculate the number of muon-neutrinos in IceCube predicted by each, while, in Section 5, we present comparative plots of the two models in parameter space. We summarise and conclude in Section 6.

2 Two models of neutrino production at AGN

AGN have long been presumed to be sites of high-energy neutrino production. In the scenario of neutrino production by meson decay, it is assumed that inside the AGN protons are accelerated through first-order Fermi shock acceleration [6, 19] and that pions are produced in the processes

$$p + \gamma \rightarrow \Delta^+ \rightarrow \begin{cases} p + \pi^0 \\ n + \pi^+ \end{cases} \quad , \qquad n + \gamma \rightarrow p + \pi^- \ , \tag{2.1}$$

with branching ratios $\mathrm{Br}\left(\Delta^+ \rightarrow p\pi^0\right) = 2/3$ and $\mathrm{Br}\left(\Delta^+ \rightarrow n\pi^+\right) = 1/3$. The neutral pions decay into gamma rays through $\pi^0 \rightarrow \gamma\gamma$, while the charged pions decay into electron- and muon-neutrinos through

$$\pi^+ \rightarrow \nu_\mu + \mu^+ \rightarrow \nu_\mu + e^+ + \nu_e + \overline{\nu}_\mu \quad , \qquad \pi^- \rightarrow \overline{\nu}_\mu + \mu^- \rightarrow \nu_\mu + e^- + \overline{\nu}_e + \nu_\mu \ . \tag{2.2}$$

The gamma rays thus created may be obscured and dispersed by the medium, and the protons will in addition be deviated by extragalactic magnetic fields on their journey to Earth. Neutrinos, on the other hand, escape from the production site virtually unaffected by interactions with the medium, so that, if their direction could be reconstructed at detection, they could point back to their sources.

If neutrinos are produced by charged pion decay, then, from eq. (2.2), the ratios of the different flavours $(\nu_x + \overline{\nu}_x)$ to the total flux are

$$\phi^0_{\nu_e} : \phi^0_{\nu_\mu} : \phi^0_{\nu_\tau} = 1 : 2 : 0 \ . \tag{2.3}$$

Under this assumption, by the time neutrinos reach Earth, standard mass-driven neutrino oscillations will have distributed the total flux equally among the three flavours so that, at detection,

$$\phi_{\nu_e} : \phi_{\nu_\mu} : \phi_{\nu_\tau} = 1 : 1 : 1 . \tag{2.4}$$

New physics effects, such as neutrino decay [20], decoherence [21], or violation of Lorentz invariance or of CPT [22–24], could in principle result in large deviations from these ratios. In the present work, we have assumed that the ratios at production and detection are given, respectively, by their standard values, eqs. (2.3) and (2.4).

In what follows, we will present in detail two representative models of UHE neutrino production at AGN, one by Koers & Tinyakov (KT) and the other by Becker & Biermann (BB), both of which make use of the apparent correlation between the directions of UHECRs and the positions of known AGN reported by the PAO in order to extrapolate the diffuse neutrino flux.

2.1 Cosmic ray flux normalisation

The preferred mechanism for cosmic-ray acceleration at AGN is first-order Fermi acceleration [6], which results in a power-law differential diffuse cosmic-ray proton spectrum,

$$\phi_p^{\mathrm{diff}}(E) \equiv \frac{dN_p}{dE} = A_p^{\mathrm{diff}} E^{-\alpha_p} , \tag{2.5}$$

with E the cosmic-ray energy at detection on Earth and A_p^{diff} an energy-independent normalisation constant. The integral of this expression,

$$\Phi_p^{\mathrm{diff}}(E_{\mathrm{th}}) = \int_{E_{\mathrm{th}}} \frac{dN_p}{dE} dE \simeq A_p^{\mathrm{diff}} (\alpha_p - 1)^{-1} E_{\mathrm{th}}^{-\alpha_p+1} , \tag{2.6}$$

is the integrated cosmic ray flux above a certain threshold energy E_{th}. Using experimental data, the integrated flux can also be calculated as

$$\Phi_p^{\mathrm{diff}}(E_{\mathrm{th}}) = N_{\mathrm{evts}}(E_{\mathrm{th}}) / \Xi , \tag{2.7}$$

where $N_{\mathrm{evts}}(E_{\mathrm{th}})$ is the number of observed cosmic rays above a given value of E_{th} and Ξ is the total detector exposure.

Combining this expression with eq. (2.6) yields for the normalisation constant,

$$A_p^{\mathrm{diff}} = \Phi_p^{\mathrm{diff}} (\alpha_p - 1) E_{\mathrm{th}}^{\alpha_p-1} = \frac{N_{\mathrm{evts}}(\alpha_p - 1)}{\Xi} E_{\mathrm{th}}^{\alpha_p-1} . \tag{2.8}$$

We will see in the following two subsections that the relation between the cosmic-ray normalisation constant, A_p^{diff}, and the neutrino normalisation constant, A_ν^{diff}, is model-dependent.

When calculating the proton spectrum from a single point source, we will need to weigh the normalisation constant using the detector effective area A that is accessible to the observation, which depends on the declination δ_s of the source, i.e.,

$$A_p^{\mathrm{pt}} = \Phi_p^{\mathrm{pt}} (\alpha_p - 1) E_{\mathrm{th}}^{\alpha_p-1} \equiv \frac{N_{\mathrm{evts}}(\alpha_p - 1)}{\Xi} E_{\mathrm{th}}^{\alpha_p-1} \frac{\int A(\delta_s) d\Omega}{A(\delta_s)} , \tag{2.9}$$

where we have implicitly defined the integrated flux from a point source,Φ_p^{pt}.

We will use the latest results from the PAO on the observation of UHECRs [7] to evaluate the diffuse and point-source cosmic-ray fluxes. Using data recorded from 1 January 2004 to 31 December 2009, amounting to an exposure of $\Xi = 20370$ km^2 yr sr, the total number of UHECRs with zenith angles $\theta \leq 60°$ and reconstructed energies above $E_{\text{th}} = 55$ EeV is $N_{\text{tot}} = 69$ events. Of these, the arrival directions of $N_{\text{corr}} = 29$ events were found to lie at an angular distance of less than $3.1°$ from the position of an AGN within 75 Mpc ($z \leq 0.018$) in the 12th edition Véron-Cetty & Véron (VCV) catalogue, i.e., they were correlated to an identified AGN. In particular, $N_{\text{Cen A}} = 2$ events were correlated to Centaurus A (Cen A), the nearest active galaxy, which, at a distance of about 3.5 Mpc, is one of the most promising UHE neutrino sources [25, 26].

Note that the original PAO report on UHECR anisotropy [8] made use of 9000 km^2 yr sr to report a total of 29 events above a threshold energy of 57 EeV, out of which 20 were correlated to AGN in the VCV catalogue, and 2 were correlated to Cen A. The neutrino production models that we have considered in our analysis were built using these data. In what follows, we have updated them using the latest PAO results.

2.2 Model by Koers & Tinyakov

The KT model [15] assumes that Cen A is a typical source of UHECRs and neutrinos, and computes the diffuse flux under the assumption that all sources are identical to Cen A by integrating over a cosmological distribution of sources, while taking into account energy losses during the propagation of the particles. Two limiting cases have been considered regarding the source distribution: one in which there is no source evolution with redshift, that is, $\epsilon(z) = 1$, and another one, adopted from [27], in which there is a strong source evolution that follows the star formation rate, i.e.,

$$\epsilon(z) \propto \begin{cases} (1+z)^{3.4} & , \text{ if } z \leq 1.9 \\ (1+1.9)^{3.4} & , \text{ if } 1.9 < z < 3 \\ (z-3)^{-0.33} & , \text{ if } z \geq 3 \end{cases} . \tag{2.10}$$

The integrated UHECR diffuse flux and the integrated flux from Cen A above 55 EeV can be calculated, respectively, using eqs. (2.8) and (2.9):

$$\Phi_p^{\text{diff}}(E_{\text{th}}) = \frac{N_{\text{tot}} - N_{\text{Cen A}}}{\Xi} = 1 \times 10^{-20} \text{ cm}^{-2} \text{ s}^{-1} \text{ sr}^{-1} \tag{2.11}$$

$$\Phi_p^{\text{Cen A}}(E_{\text{th}}) = \frac{N_{\text{Cen A}}}{\Xi} \frac{\int A(\delta_s) d\Omega}{A(\delta_s)} = 2 \times 10^{-21} \text{ cm}^{-2} \text{ s}^{-1} , \tag{2.12}$$

where $\delta_s = -43°$ is the declination of Cen A. The relative exposure at this declination is $A(\delta_s) / \int A(\delta_s) d\Omega = 0.15$ sr^{-1} [15, 28]. In eq. (2.11), the number of cosmic rays from Cen A is subtracted from the total since the flux is not subject to the energy losses that the diffuse flux is, on account of its being the closest AGN.

The diffuse neutrino flux is normalised using the integrated UHECR flux $\Phi_p^{\text{diff}}(E_{\text{th}})$ above the threshold E_{th},

$$\frac{\phi_\nu^{\text{diff}}(E_\nu)}{\phi_\nu^{\text{Cen A}}(E_\nu)} = H(E_{\text{th}}) \frac{\Phi_p^{\text{diff}}(E_{\text{th}})}{\Phi_p^{\text{Cen A}}(E_{\text{th}})} \simeq 5H(E_{\text{th}}) . \tag{2.13}$$

The proportionality constant, $H(E_{\text{th}})$, is called the "neutrino boost factor" and contains the information on neutrino mean free path lengths and source evolution. To calculate it, proton

energy losses are taken into account in the continuous-loss approximation, considering losses by the adiabatic expansion of the Universe and from interactions with the CMB photons resulting in pion photoproduction and electron-positron pair production; see Appendix A in Ref. [15] for details. The variation of H with α_p is shown in the same reference. Note that the change in the reconstructed threshold energy from 57 EeV in the original PAO analysis [8] to 55 EeV in the updated analysis [7] has reduced H in about 10%. This decrease is compensated by a higher value of the ratio $\Phi_p^{\text{diff}}/\Phi_p^{\text{Cen A}}$, which has moved from 1.8 using the original PAO data to 5 using the latest data. As a result, the KT diffuse neutrino flux has only changed marginally between the old and new PAO data set. To obtain the diffuse flux, the source distribution is integrated up to $z = 5$. This relation between the diffuse neutrino flux and the flux from Cen A is the main result of the KT model.

In their paper [15], Koers & Tinyakov used a model by Cuoco & Hannestad [29] to describe the neutrino emission from Cen A, $\phi_\nu^{\text{Cen A}}$, itself based on a model by Mannheim, Protheroe & Rachen [30]. In this model, it is assumed that high-energy protons, accelerated by some mechanism (e.g., shock acceleration) are confined within a region close to the source. Because of energy losses in their photopion interactions with the ambient photon field, which is assumed to have an energy spectrum $n(E_\gamma) \propto E_\gamma^{-2}$, their lifetime is much shorter than their diffusive escape time and they decay into neutrons and neutrinos, both of which escape the source. Thereafter, the neutrons decay into UHECR protons; however, because of their interaction with the photon field before decaying, the neutrons produce a softer proton spectrum than the seed proton spectrum. Furthermore, the model predicts two spectral breaks in the CR spectrum, at energies at which the optical depths for proton and neutrino photopion production become unity. These two breaks are close in energy, though, so that, to simplify the model, only one spectral break is considered, at energy E_{br}. Below E_{br}, the UHECR proton and neutrino spectra are harder than the seed proton spectrum by one power of the energy, while above E_{br}, the UHECR proton spectrum is softer than the seed spectrum by one power of the energy and the neutrino spectrum is harder by one power of the energy. Hence, at high energies, the model predicts a neutrino spectrum that is harder by one power of the energy than the UHECR proton spectrum.

Following [15, 29, 30], the all-flavour neutrino spectrum from Cen A can be written as

$$\phi_{\nu_{\text{all}}}^{\text{Cen A}}(E_\nu) = \frac{\xi_\nu}{\xi_n \eta_{\nu n}^2} \min\left(\frac{E_\nu}{\eta_{\nu n} E_{\text{br}}}, \frac{E_\nu^2}{\eta_{\nu n}^2 E_{\text{br}}^2}\right) \phi_p^{\text{Cen A}}\left(\frac{E_\nu}{\eta_{\nu n}}\right) \ , \tag{2.14}$$

where ξ_i $(i = \nu, n)$ is the fraction of the proton's energy that is transferred to the species i in photopion interactions and $\eta_{\nu n}$ is the ratio of the average neutrino energy to the average neutron energy. The KT model uses for these parameters the values featured in [30], obtained from Monte Carlo simulations: $\xi_\nu \approx 0.1$, $\xi_n \approx 0.5$, $\langle E_\nu \rangle / E_p \approx 0.033$ and $\langle E_n \rangle / E_p \approx 0.83$, with which $\xi_\nu / \xi_n = 0.2$ and $\eta_{\nu n} = 0.04$. The neutrino break energy, E_{br}, is estimated from the gamma-ray break energy as $E_{\text{br}} \simeq 3 \times 10^8 E_{\gamma,\text{br}}$. Ref. [30] uses $E_{\gamma,\text{br}} = 200$ MeV, so that $E_{\text{br}} = 10^8$ GeV. Under the assumption of equal flavour ratios at Earth, eq. (2.4), the $\nu_\mu + \overline{\nu}_\mu$ flux is $1/3$ the flux in eq. (2.14). Plugging the power-law proton spectrum, eq. (2.5), with the normalisation constant for a point source, eq. (2.9), into the eq. (2.14) yields

$$\phi_{\nu_\mu}^{\text{Cen A}}(E_\nu) = \frac{\Phi_p^{\text{Cen A}}(E_{\text{th}})}{3} \frac{\xi_\nu \eta_{\nu n}^{\alpha_p - 2}}{\xi_n} \frac{\alpha_p - 1}{E_{\text{th}}} \left(\frac{E_\nu}{E_{\text{th}}}\right)^{-\alpha_p} \left(\frac{E_\nu}{E_{\nu,\text{br}}}\right) \min\left(1, \frac{E_\nu}{E_{\nu,\text{br}}}\right) \tag{2.15}$$

for the muon-neutrino flux from Cen A, with $E_{\nu,\text{br}} \equiv \eta_{\nu n} E_{\text{br}} = 4 \times 10^6$ GeV. Using the scaling relation, eq. (2.13), the muon-neutrino diffuse flux in the KT model is therefore

$\phi_{\nu_\mu}^{\mathrm{diff,KT}}(E_\nu) \simeq 5H(E_{\mathrm{th}})\phi_{\nu_\mu}^{\mathrm{Cen\ A}}(E_\nu)$ and we can write it as

$$\phi_{\nu_\mu}^{\mathrm{diff,KT}}(E_\nu) = A_\nu^{\mathrm{diff,KT}}E_\nu^{-\alpha}\min\left(\frac{E_\nu}{E_{\nu,\mathrm{br}}},\frac{E_\nu^2}{E_{\nu,\mathrm{br}}^2}\right)\ ,\tag{2.16}$$

with the neutrino normalisation given by

$$A_\nu^{\mathrm{diff,KT}} \simeq \frac{5}{3}H(E_{\mathrm{th}})\frac{\xi_\nu}{\xi_n}\eta_{\nu n}^{\alpha_p-2}A_p^{\mathrm{Cen\ A}}(\alpha_p)\ ,\tag{2.17}$$

and, following eq. (2.9), $A_p^{\mathrm{Cen\ A}} = \Phi_p^{\mathrm{Cen\ A}}(\alpha_p-1)E_{\mathrm{th}}^{\alpha_p-1}$.

2.3   Model by Becker & Biermann

The BB model [16] describes the production of high-energy neutrinos in the relativistic jets of radio galaxies. According to the model, the UHECRs observed by the PAO originated at FR-I galaxies (relatively low-luminosity radio galaxies with extended radio jets, and radio knots distributed along them), which can in principle accelerate protons up to about 10^{20} eV. Like in the KT model, here the protons are also shock-accelerated. Unlike the KT model, though, where the neutrino emission occurred in a region close to the AGN core, in the BB model the neutrino emission from $p\gamma$ interactions is expected to peak at the first strong shock along the jet, lying at a distance of $z_j \sim 3000$ gravitational radii from the center.

The optical depth corresponding to proton interactions with the disc photon field $\tau_{p\gamma_{disc}} \approx 0.02$ and so $p\gamma$ interactions in the disc are not the dominant source of neutrinos. The proton-proton interactions that occur when the jet encounters the AGN's torus are also neglected as neutrino source in the BB model. The dominant mechanism of neutrino production is the interaction between the accelerated protons and the synchrotron photons in the relativistic jet, at one of the jet's knots. For boost factors of the streaming plasma of $\Gamma \sim 10$, the optical depth $\tau_{p\gamma_{\mathrm{synch}}} \sim 1$.

Hence, it is expected that neutrino emission occurs predominantly at the foot of the jet, where the beam is still highly collimated. Therefore, the BB model predicts a highly beamed neutrino emission, produced in the first shock ($z_j \sim 3000 r_g$), and consequently observable only from sources whose jets are directed towards Earth. Flat-spectrum radio sources, such as FR-I galaxies whose jets are pointing towards Earth, will have correlated neutrino and proton spectra, while steep-spectrum sources, which are AGN seen from the side, are expected to be weak neutrino sources, but to contribute to the cosmic-ray proton flux.

The BB model assumes that the $N_{\mathrm{corr}} = 29$ events that were observed by the PAO to have a positional correlation to sources in the VCV catalogue were indeed originated at AGN lying in the supergalactic plane. In order to relate the proton and neutrino normalisation constants, A_p^{diff} and A_ν^{diff}, we will use the connection between the proton and neutrino energy fluxes [16], i.e.,

$$j_\nu = \frac{\tau_{p\gamma}}{12}\frac{\Gamma_\nu}{\Gamma_{\mathrm{CR}}}\frac{\Omega_p}{\Omega_\nu}\frac{n_\nu}{n_p}(z_{\mathrm{CR}}^{\max})j_p\ ,\tag{2.18}$$

where Ω_ν, Ω_{CR} are the solid angles of emission of neutrinos and cosmic rays, respectively, and Γ_ν, Γ_{CR} are the boost factors of neutrinos and cosmic rays, respectively. The parameter $z_{\mathrm{CR}}^{\max}$ is the redshift of the farthest AGN that contribute to the cosmic-ray flux. The total number of neutrino (proton) sources, n_ν (n_p), is calculated by integrating the luminosity function of Willott [31] (Dunlop & Peacock [32]) from $z_{\mathrm{CR}}^{\min} = 0.018$ (0.0008) up to $z_{\mathrm{CR}}^{\max}$.

On the other hand, assuming a power-law behaviour for the diffuse differential flux of protons, eq. (2.5), the energy flux results in

$$j_p = A_p \int_{E_{p,\min}}^{E_{p,\max}} E_p \frac{dN_p}{dE_p} \, dE_p = \begin{cases} A_p \left(\alpha_p - 2\right)^{-1} E_{p,\min}^{-\alpha_p+2} & , \text{ if } \alpha_p \neq 2 \\ A_p \ln\left(E_{p,\max}/E_{p,\min}\right) & , \text{ if } \alpha_p = 2 \end{cases} , \qquad (2.19)$$

where the term proportional to $E_{p,\max}^{-\alpha_p+2}$ has been neglected, in the case when $\alpha_p \neq 2$. Assuming that the neutrino spectrum follows the proton spectrum, i.e., $\phi_{\nu_\mu}^{\mathrm{diff,BB}} = A_\nu^{\mathrm{diff}} E_\nu^{-\alpha_\nu}$ with $\alpha_\nu \approx \alpha_p$, the energy flux for neutrinos is

$$j_\nu \simeq \begin{cases} A_\nu^{\mathrm{diff}} \left(\alpha_p - 2\right)^{-1} E_{\nu,\min}^{-\alpha_p+2} & , \text{ if } \alpha_p \neq 2 \\ A_\nu^{\mathrm{diff}} \ln\left(E_{\nu,\max}/E_{\nu,\min}\right) & , \text{ if } \alpha_p = 2 \end{cases} . \qquad (2.20)$$

The lower integration limits for protons and neutrinos are, respectively, $E_{p,\min} = \Gamma_p m_p \approx \Gamma_p \cdot (1 \text{ GeV})$ and $E_{\nu,\min} = \Gamma_\nu \cdot (m_\pi/4) = \Gamma_\nu \cdot (0.035 \text{ GeV})$. Finally, replacing eq. (2.19), eq. (2.20), and the proton normalisation constant A_p^{diff} given by eq. (2.8) evaluated with $N_{\mathrm{evts}} = N_{\mathrm{corr}}$, we see that when $\alpha_p \neq 2$, the neutrino normalisation constant is

$$A_\nu^{\mathrm{diff,BB}} \simeq \frac{\tau_{p\gamma}}{12} \left(\frac{\Gamma_\nu}{\Gamma_p}\right)^{\alpha_p+1} \frac{n_\nu}{n_p} \left(z_{\mathrm{CR}}^{\max}\right) \left(\frac{m_\pi}{4}\right)^{\alpha_p-2} A_p^{\mathrm{diff}} \left(\alpha_p\right) . \qquad (2.21)$$

The dependence of n_ν/n_p on $z_{\mathrm{CR}}^{\max}$ is shown graphically in Figure 5 of Ref. [16]: n_ν/n_p decreases with $z_{\mathrm{CR}}^{\max}$. To arrive at this expression[1], it must be noted that because of the relativistic beaming in the jets, the emission solid angles are $\Omega_\nu \sim 1/\Gamma_\nu^2$ and $\Omega_p \sim 1/\Gamma_{\mathrm{CR}}^2$. When $\alpha_p = 2$, the logarithms in the two spectra are similar and cancel out, making the previous expression for $A_\nu^{\mathrm{diff,BB}}$ valid also for $\alpha_p = 2$. Note that, since the ratio N_{corr}/Ξ has decreased approximately by a factor of 2 between the original and updated PAO analyses, then the updated BB diffuse flux is about half the original.

3 Current and preliminary bounds on the neutrino flux

In the present work, we have assumed that the UHE AGN neutrino flux accounts for all of the UHE neutrino flux. This is, of course, a simplifying assumption, since high-energy contributions could also originate at other types of sources, such as gamma-ray bursts [33–36].

We have taken into account three experimental bounds on the diffuse astrophysical neutrino flux: two upper bounds, one set by the AMANDA-II experiment and the other by its successor, IceCube, in its half-completed configuration of 40 DOM strings; and a lower bound given by the discovery potential of the final 86-string IceCube configuration. These three bounds have been included in figure 1.

The AMANDA-II upper bound on the diffuse high-energy flux of extra-terrestrial muon-neutrinos was obtained by using data recorded between the years 2000 and 2004 [38]:

$$E_\nu^2 \phi_{\nu_\mu}^{\mathrm{diff}} \leq 7.4 \times 10^{-8} \text{ GeV cm}^{-2} \text{ s}^{-1} \text{ sr}^{-1} \, (90\% \text{ C.L.}) , \qquad (3.1)$$

in the range 16 TeV – 2.5 PeV. This bound was set using exclusively upgoing UHE neutrinos, six of which were detected during the 807 days of live time reported.

---

[1]The reader should be wary that in their paper [16], Becker & Biermann incorrectly reported a dependence of the form $\sim \left(\Gamma_\nu/\Gamma_{\mathrm{CR}}\right)^{5-\alpha_p}$ due to an algebraic mistake[37].

More recently, the IceCube Collaboration presented a preliminary upper bound using 375 days of recorded upgoing data with the half-completed IceCube-40 array which is almost an order of magnitude tighter than the AMANDA bound [39]:

$$E_\nu^2 \phi_{\nu_\mu}^{\text{diff}} \leq 8 \times 10^{-9} \text{ GeV cm}^{-2} \text{ s}^{-1} \text{ sr}^{-1} \, (90\% \text{ C.L.}) \;, \qquad (3.2)$$

in the range $10^{4.5} - 10^7$ GeV.

Finally, the discovery potential at the 5σ level of the full, 86-string, IceCube array has been recently estimated [40] to reach, after five years of exposure,

$$E_\nu^2 \phi_{\nu_\mu}^{\text{diff}} \leq 7 \times 10^{-9} \text{ GeV cm}^{-2} \text{ s}^{-1} \text{ sr}^{-1} \, (5\sigma) \;, \qquad (3.3)$$

also in the range $10^{4.5} - 10^7$ GeV. This is the estimated minimum necessary flux required for a 5σ discovery after five years of running IC86. We will use this discovery potential as a lower bound on the neutrino flux. The discovery potential in eq. (3.3) is better than the original estimate of 9.9×10^{-9} GeV cm^{-2} s^{-1} sr^{-1} that was presented in [41] due to a better knowledge of the detector and improved simulations.

Note that these three bounds were obtained under the assumption of an $E_\nu^{-\alpha}$ neutrino flux, with $\alpha = 2$. For the KT and BB models in our work, however, we have allowed for $\alpha \neq 2$. Therefore, we have calculated for each one of them the associated number of muon-neutrinos in the AMANDA, IceCube-40 and IceCube-86 configurations, as appropriate, by assuming an E_ν^{-2} flux, and used these derived bounds on the number of events, and not on the flux, to constrain the KT and BB models. Concretely, we have assumed a $\phi_{\nu_\mu}^{\text{diff}}(E_\nu) = k E_\nu^{-2}$ flux, with the normalisation, k, given in each case by the numerical value of the bounds in eqs. (3.1)-–(3.3), in units of GeV^{-1} cm^{-2} s^{-1} sr^{-1}. These numbers are displayed in table 1. The expressions required to calculate the number of upgoing muon-neutrinos in the AMANDA, IceCube-40, and IceCube-86 arrays, for an arbitrary diffuse neutrino flux $\phi_{\nu_\mu}^{\text{diff}}$, are contained in Appendix A. We have assumed that the effective detector area of AMANDA is 1/100 times that of IceCube-86 and that the effective area of IceCube-40 is half the area of IceCube-86, on account of half the number of strings having been deployed. Note, however, that this is only an estimate, since the actual effective area of IceCube-40 will be strongly dependent on the efficiency of the cuts employed to calculate it.

4   Muon-neutrino number of events in the IceCube-86 detector for the BB and KT models

In this Section, we study the Koers & Tinyakov (KT) and the Becker & Biermann (BB) models of diffuse AGN neutrino flux through their predictions of the number of muon-neutrinos that will be detected by the full IceCube-86 neutrino detector. To calculate the number of neutrinos, we have adopted the method followed in [15], which is summarised here in Appendix A.

In our analysis, we have fixed the IceCube-86 detector exposure time at $T = 5$ years and calculated the integrated event yield within the energy range $10^5 - 10^8$ GeV. Only upgoing neutrinos have been considered, i.e., those that reach the detector with zenith angles between $90°$ and $180°$ (the normal to the South Pole lies at $0°$), for which the atmospheric neutrino and muon background is filtered out by interactions inside the Earth. Downgoing neutrinos, i.e., those with zenith angles between $0°$ and $90°$, traverse only about 10 km of atmosphere before reaching the detector and have not been included in the analysis due to the added

Limit	Energy range [GeV]	Exp. time	Upgoing ν_μ
AMANDA upper bound (AMANDA) [38]	$1.6 \times 10^4 - 2.5 \times 10^6$	807 days	6.0
IceCube-40 preliminary upper bound (IC40) [39]	$10^{4.5} - 10^7$	375 days	5.90
IceCube-86 estimated 5σ discovery (IC86) [40]	$10^{4.5} - 10^7$	5 years	50.28

Table 1. Maximum number of upgoing muon-neutrinos allowed by the reported exclusion limit from AMANDA and the preliminary one from IceCube-40, and minimum number of events needed for 5σ discovery according to the estimated IceCube-86 5-year discovery flux. In every case, the event numbers were calculated by assuming a E_ν^{-2} diffuse flux. Each bound on the number of events was calculated in the respective detector configuration (Appendix A contains the effective area for each), with the corresponding exposure time.

Limit	no source evolution	strong source evolution
AMANDA	3.04	2.81
IC40	2.59	2.27
IC86	2.57	2.25

Table 2. Maximum value of the spectral index α in the Koers-Tinyakov model allowed by the upper bounds AMANDA and IC40, and minimum value needed for 5σ discovery according to the estimated IC86 discovery potential.

difficulty of separating the atmospheric background from the astrophysical neutrino signal. Furthermore, in the case of the KT flux, we have considered both the scenario with no source evolution and the one with strong source evolution.

Based on the experimental bounds introduced in the previous Section, we have defined two visibility criteria with the purpose of identifying the regions of parameter space allowed by the upper limits and accessible by the discovery potential of the full IceCube-86 array. Under the first one –the AMANDA visibility criterion–, the IceCube-86 event-rate predictions, for either KT or BB, are required to lie above the IC86 discovery potential and below the AMANDA upper bound. Similarly, under the IC40 visibility criterion, the event rates must lie above the IC86 discovery potential and below the IC40 upper bound.

4.1 Parameters under study and neutrino fluxes

We have calculated our expectations of the neutrino flux models taking as free parameters α for the KT model (to simplify, we will use $\alpha \equiv \alpha_p$ hereafter), and α, Γ_ν/Γ_{CR}, and z_{CR}^{max} for the BB model, and varied them within the following intervals:

$$2 \le \alpha \le 3 \ , \qquad 1 \le \Gamma_\nu/\Gamma_{CR} \le 20 \ , \qquad 10^{-3} \le z_{CR}^{max} \le 0.03 \ . \qquad (4.1)$$

This range of α has been chosen in order to cover a wide range around 2.7, the preferred value obtained from fits to combined cosmic-ray data [42], or values less than 2.3 that are predicted in case of stochastic shock acceleration [43–47]. We have defined the range of Γ_ν/Γ_{CR} for values greater than 1 since, under the assumptions made by the BB model, the neutrinos are produced in early shocks and protons, in late ones. Besides, it includes the value of 3 used in [16]. The range of z_{CR}^{max} is the same as the one used in said reference. Our purpose in varying the latter parameter, z_{CR}^{max}, is to test different hypotheses about the maximum redshift up to which the AGN contribute to the UHE diffuse neutrino flux. We remind the reader that the
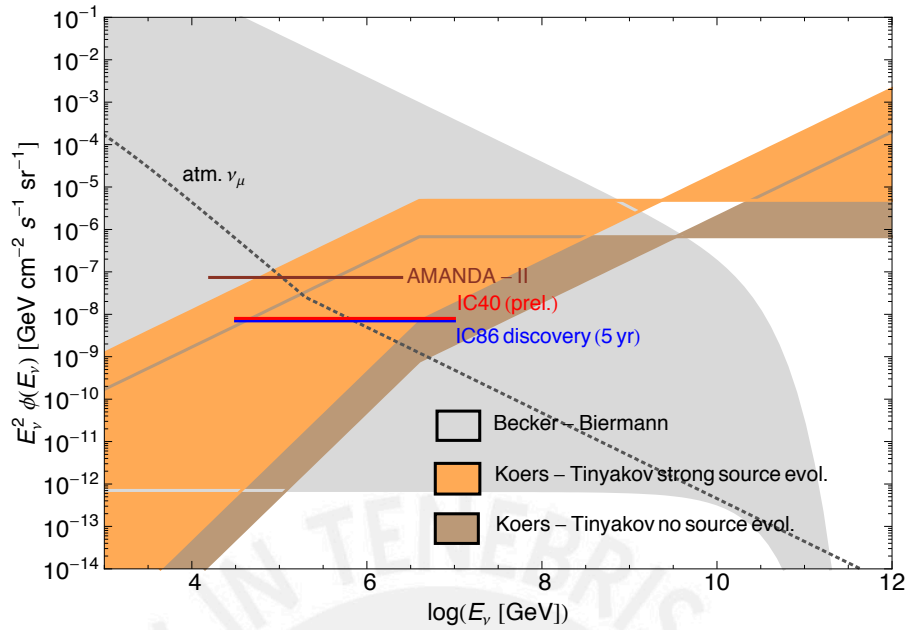
Figure 1. AGN muon-neutrino fluxes, multiplied by E_ν^2, according to the models by Becker & Biermann (BB) and Koers & Tinyakov (KT), with strong source evolution and without source evolution. The regions were generated by varying the model parameters in the ranges $2 \leq \alpha \leq 3$, $1 \leq \Gamma_\nu/\Gamma_{\rm CR} \leq 20$, and $10^{-3} \leq z_{\rm CR}^{\rm max} \leq 0.03$. The grey region corresponds to all the possible BB fluxes resulting from the variation of α, $\Gamma_\nu/\Gamma_{\rm CR}$, and $z_{\rm CR}^{\rm max}$, whereas the brown and orange regions correspond to all the possible KT fluxes resulting from the variation of α, under the assumption of no source evolution and of strong source evolution, respectively. The atmospheric muon-neutrino flux has been plotted (in black, dotted, lines) for comparison. The AMANDA-II upper bound, the preliminary 40-string IceCube upper bound and an estimated 86-string IceCube five-year discovery potential at 5σ have been included by assuming a E_ν^{-2} flux. The atmospheric neutrino flux is given by the parametrisation in Ref. [15]. See the text for details.

results for the KT model have been obtained for a fixed value of $z_{\rm CR}^{\rm max} = 5$ and so they were not affected by this variation.

Figure 1 shows the BB and KT diffuse muon-neutrino fluxes, multiplied by E_ν^2, as functions of the neutrino energy, when the values of the model parameters are varied within the ranges that we have quoted above. We have also included the upper bounds on the flux set by AMANDA and IceCube-40, and the estimated discovery potential of IceCube-86 after five years of running. Our analysis will focus on the different regions enclosed between these upper bounds and the IC86 discovery potential taken as a lower bound, in the energy range 10^5–10^8 GeV, where the fluxes may be detected in IceCube. We will find how the bounds on the neutrino flux translate into bounds on the values of α, $\Gamma_\nu/\Gamma_{\rm CR}$, and $z_{\rm CR}^{\rm max}$, thus restricting the capacity of the KT and BB flux models to account for an observed extra-terrestrial neutrino signal.

4.2 KT event-rate expectations in IceCube-86

Since the KT flux depends on a single parameter, i.e., the spectral index α, we can translate the bounds on event numbers directly into bounds on α. In this way, the results presented
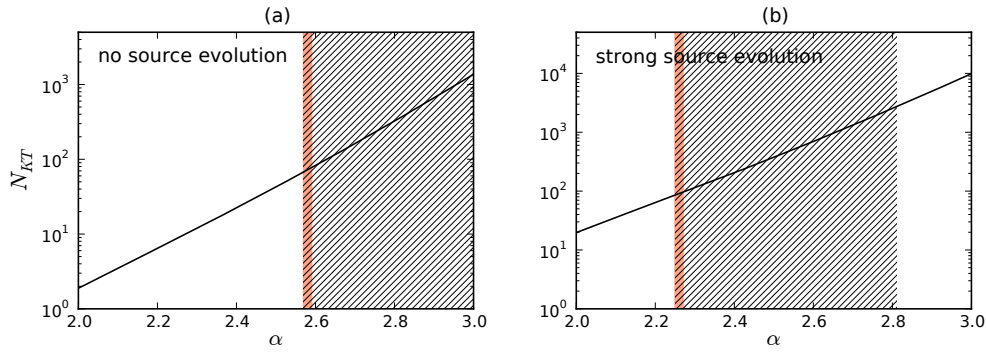
Figure 2. Integrated number of upgoing muon-neutrinos, between 10^5 and 10^8 GeV, expected in IceCube-86, after $T = 5$ years of exposure, associated to the KT production model assuming (a) no source evolution and (b) strong source evolution. The orange-coloured bands are the regions of values of α that lies above the IC86 discovery potential and below the IC40 upper bound, while the hatched region lies above IC86 and below the AMANDA upper bound (see table 2).

in table 2 represent the upper limits on α given by the AMANDA and IC40 bounds and the lower limits given by the IC86 discovery potential.

Figure 2 shows the integrated number of upgoing muon-neutrinos with energies between 10^5 and 10^8 GeV, as a function of α, that is expected in the full 86-string IceCube array after five years of exposure. Plot (a) assumes no source evolution, whereas (b) assumes strong source evolution. The predictions under the assumption of strong source evolution are up to an order of magnitude higher than under no source evolution. This fact can be easily understood since a difference of a similar magnitude is found in the neutrino boost factor, as shown in Ref. [15].

The orange-coloured and hatched bands mark the visibility regions under the IC40 and AMANDA visibility criteria, respectively, according to table 2. Owing to the fact that the AMANDA upper bound is less restrictive than the IC40 bound, the visibility regions are in every case larger when the former one is used. According to figure 2 and table 2, the ranges of event numbers, N_{KT}, that IceCube-86 will be able to detect in the interval $10^5 - 10^8$ GeV, after five years of exposure, are:

$$68 \leq N_{\mathrm{KT}}^{\mathrm{up}} \leq 77\,(1847)\ ,\qquad(4.2)$$

assuming no source evolution and using the IC40 (AMANDA) upper bound, and

$$85 \leq N_{\mathrm{KT}}^{\mathrm{up}} \leq 95\,(2709)\ ,\qquad(4.3)$$

assuming strong source evolution.

From table 2, we see that the KT model with no source evolution is allowed for higher values of α than the model with strong source evolution. This is due to the fact that the KT flux grows with α, and that, for a given value of α, the event yield produced by the strong source evolution model is up to an order of magnitude higher than the yield with no source evolution. Thus, lower values of α are needed to keep the former below the IC40 or AMANDA event-number upper bounds.

From the same table, we find that for the KT model the value of $\alpha = 2.7$, obtained from fits to cosmic-ray data, would still be allowed under the AMANDA visibility criterion, but
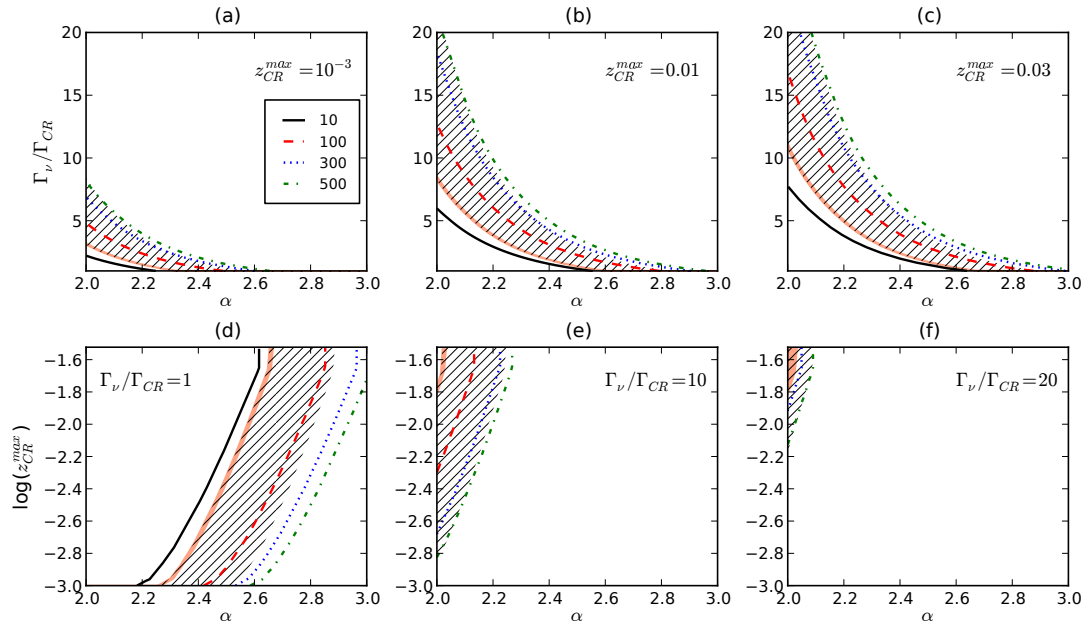
Figure 3. Variation of the integrated number of upgoing muon-neutrinos expected in the range $10^5 \leq E_\nu/\text{GeV} \leq 10^8$ associated to the BB model, after $T = 5$ years of exposure of the IceCube-86 detector. In (a), (b), and (c), the value of $z_{\text{CR}}^{\max}$ has been fixed, respectively, at the representative values of 10^{-3}, 0.01, and 0.03, while α and $\Gamma_\nu/\Gamma_{\text{CR}}$ have been allowed to vary. Likewise, in (d), (e), and (f), $\Gamma_\nu/\Gamma_{\text{CR}}$ has been fixed at 1, 10, and 20, respectively, while α and $z_{\text{CR}}^{\max}$ have been varied. The solid lines are iso-contours of number of events: 10 (solid black), 100 (dashed red), 300 (dotted blue), and 500 (dash-dotted green). The region coloured orange is the parameter region where the event-number predictions lie above the IC86 discovery potential and below the IC40 upper bound, i.e., the IC40 visibility region. Similarly, the hatched region is where the predictions lie above the IC86 potential and below the AMANDA upper bound, i.e., the AMANDA visibility region.

is discarded by the more recent IC40 criterion, regardless of the choice of source evolution. Under the assumption of strong source evolution, the other proposed value of $\alpha = 2.3$ is excluded (permitted) by the IC40 (AMANDA) visibility criterion, while values of $\alpha \leq 2.25$ would be out of reach of the IceCube discovery potential. Under no source evolution, the region of α below the IC86 potential starts from 2.57. This constitutes a strong hint toward the KT flux being too large. However, as explained in Section 3, we would like to stress that our visibility criteria make use of event-yield bounds that are deduced from bounds on a E_ν^{-2} flux, a comparison that might be overly reducing the size of the visibility regions. A more sophisticated analysis that makes use of model-independent flux bounds, i.e., bounds not exclusive to E_ν^{-2} models, will be presented elsewhere [48].

4.3 BB event-rate expectations in IceCube-86

As to the BB flux model, figure 3 shows iso-contours of the expected integrated number of upgoing muon-neutrinos in the IceCube-86 detector, in the $\Gamma_\nu/\Gamma_{\text{CR}}$–$\alpha$ plane, for fixed values of (a) $z_{\text{CR}}^{\max} = 10^{-3}$, (b) 0.01, and (c) 0.03, and in the $z_{\text{CR}}^{\max}$–α plane, for fixed values of (d) $\Gamma_\nu/\Gamma_{\text{CR}} = 1$, (e) 10, and (f) 20. The BB normalisation constant, according to eq. (2.21),

$z_{\rm CR}^{\max}$	Minimum	Maximum α		Minimum	Maximum $\Gamma_\nu/\Gamma_{\rm CR}$	
	α	IC40 visib.	AMANDA visib.	$\Gamma_\nu/\Gamma_{\rm CR}$	IC40 visib.	AMANDA visib.
10^{-3}	2	2.3	2.65	1	3	7.5
0.01	2	2.6	2.95	1	8.5	20
0.03	2	2.65	3	1	11	20

Table 3. Allowed intervals of α and $\Gamma_\nu/\Gamma_{\rm CR}$ obtained by projecting the visibility regions from plots 3a–c onto the axes.

$\Gamma_\nu/\Gamma_{\rm CR}$	Minimum	Maximum α		Minimum $z_{\rm CR}^{\max}$		Maximum $z_{\rm CR}^{\max}$
	α	IC40 visib.	AMANDA visib.	IC40 visib.	AMANDA visib.	
1	2.25	2.65	2.9	10^{-3}	10^{-3}	0.03
10	2	2.03	2.22	0.015	0.002	0.03
20	2	2.03	2.1	0.015	0.008	0.03

Table 4. Allowed intervals of α and $z_{\rm CR}^{\max}$ obtained by projecting the visibility regions from plots 3d–f onto the axes.

decreases with $z_{\rm CR}^{\max}$ and increases with $\Gamma_\nu/\Gamma_{\rm CR}$. This behaviour is observed in figure 3, where, for fixed values of α and $\Gamma_\nu/\Gamma_{\rm CR}$, the number of events decreases as $z_{\rm CR}^{\max}$ increases. On the other hand, for fixed values of α and $z_{\rm CR}^{\max}$, the number of events increases with $\Gamma_\nu/\Gamma_{\rm CR}$.

In each plot, as we have mentioned before, the IC40 visibility region is coloured orange and lies between the IC86 discovery potential (left border) and the IC40 upper bound (right border) listed in table 1. The AMANDA visibility region, on the other hand, is represented by the hatched region, and its right border is fixed instead by the AMANDA bound.

Besides the observed narrowness of the visibility regions, there are two main features to point out. First, if the value of $z_{\rm CR}^{\max}$ increases, the allowed ranges of α and $\Gamma_\nu/\Gamma_{\rm CR}$ also increase, with higher values being allowed. Second, if the value of $\Gamma_\nu/\Gamma_{\rm CR}$ increases, the allowed ranges of α and $z_{\rm CR}^{\max}$ decrease, with α tending to lower values and $z_{\rm CR}^{\max}$ to higher ones. These observations can be quantified if we project the visibility regions in each plane onto the horizontal and vertical axes. The allowed regions of the parameters are shown in tables 3 and 4.

In light of the results presented in these tables, and momentarily assuming that $\alpha = 2.7$ is the true value of the cosmic-ray spectral index [42], we see that under the AMANDA visibility criterion the BB flux model is clearly excluded for $\Gamma_\nu/\Gamma_{\rm CR} \gtrsim 10$ (for any value of $z_{\rm CR}^{\max}$) and also for the lowest values of $z_{\rm CR}^{\max}$, close to 10^{-3} (for any value of $\Gamma_\nu/\Gamma_{\rm CR}$). Whenever $\alpha = 2.7$ is allowed by the BB model, it is only inside a very narrow region of parameter space, around $\Gamma_\nu/\Gamma_{\rm CR} \sim 1$ and $z_{\rm CR}^{\max} \gtrsim 0.004$. On the other hand, under the more recent IC40 visibility criterion, the BB model at $\alpha = 2.7$ is discarded for all values of $\Gamma_\nu/\Gamma_{\rm CR}$ and $z_{\rm CR}^{\max}$.

If we consider the other values of $\alpha = 2.3$ and 2.0 proposed in the literature (see Ref. [16] and references therein), we find that the allowed regions, for $\alpha = 2.3$ and the AMANDA visibility criterion, are: $1 \lesssim \Gamma_\nu/\Gamma_{\rm CR} \lesssim 3$, $2.5 \lesssim \Gamma_\nu/\Gamma_{\rm CR} \lesssim 6.5$ and $3 \lesssim \Gamma_\nu/\Gamma_{\rm CR} \lesssim 8$ for $z_{\rm CR}^{\max} = 10^{-3}, 0.01$ and 0.03, respectively. In the case of $\alpha = 2$, and the AMANDA visibility criterion, the allowed regions are: $3 \lesssim \Gamma_\nu/\Gamma_{\rm CR} \lesssim 8$, $8 \lesssim \Gamma_\nu/\Gamma_{\rm CR} \lesssim 20$ and $11 \lesssim \Gamma_\nu/\Gamma_{\rm CR} \lesssim 20$ for $z_{\rm CR}^{\max} = 10^{-3}, 0.01$ and 0.03, respectively. For $\alpha = 2.3(2.0)$, and the IC40 visibility criterion, the allowed values for $\Gamma_\nu/\Gamma_{\rm CR}$ are: $1(3), 2.5(8)$ and $3(11)$ for $z_{\rm CR}^{\max} = 10^{-3}, 0.01$ and
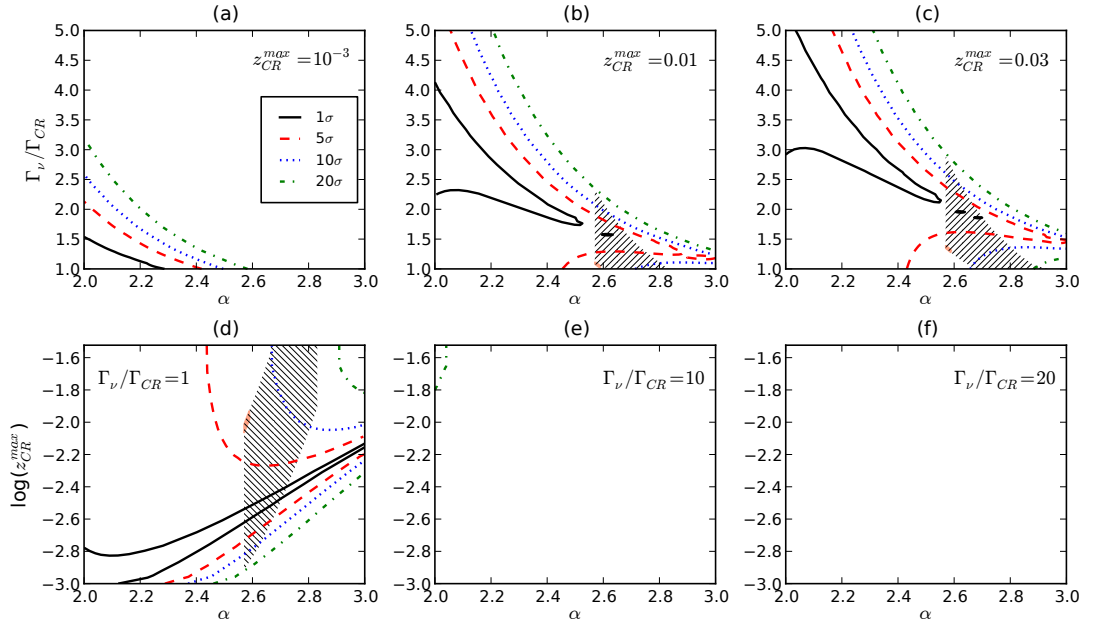
Figure 4. Separation between the BB and KT models, in terms of $\Delta \equiv |N_{\mathrm{BB}} - N_{\mathrm{KT}}|$, measured in units of $\sigma \equiv \sqrt{N_{\mathrm{KT}}}$ (see text), for upgoing neutrinos with energies in the range $10^5 \leq E_\nu/\mathrm{GeV} \leq 10^8$ and assuming no source evolution for the KT model. The exposure time $T = 5$ years. In (a), (b), and (c), the value of $z_{\mathrm{CR}}^{\mathrm{max}}$ has been fixed, respectively, at the representative values of 10^{-3}, 0.01, and 0.03, while α and $\Gamma_\nu/\Gamma_{\mathrm{CR}}$ have been allowed to vary. Likewise, in (d), (e), and (f), $\Gamma_\nu/\Gamma_{\mathrm{CR}}$ has been fixed at 1, 10, and 20, respectively, while α and $z_{\mathrm{CR}}^{\mathrm{max}}$ have been varied. The solid lines are iso-contours of $\Delta = 1\sigma$ (solid black), 5σ (dashed red), 10σ (dotted blue), and 20σ (dash-dotted green). The region coloured orange is the parameter region where the event-number predictions of, simultaneously, the KT and BB models lie above the IC86 discovery potential and below the IC40 upper bound, i.e., the IC40 visibility region. Similarly, the hatched region is where the predictions of both models lie above the IC86 potential and below the AMANDA upper bound, i.e., the AMANDA visibility region. These regions of simultaneous visibility are where comparison between the two production models is meaningful, according to each of the two visibility criteria.

0.03, respectively. Clearly, lower values of α fare better under the more recent IC40 upper bound. Like for the KT model, the BB model region of parameter space could be larger if an analysis based on non-E_ν^{-2} bounds were performed instead.

5   Comparison between the KT and BB models using the IceCube detector

We have quantified the difference between the predictions put forward by the two models using the quantity

$$\Delta\left(\alpha, \Gamma_\nu/\Gamma_{\mathrm{CR}}, z_{\mathrm{CR}}^{\mathrm{max}}\right) = \left|N_{\mathrm{BB}}\left(\alpha, \Gamma_\nu/\Gamma_{\mathrm{CR}}, z_{\mathrm{CR}}^{\mathrm{max}}\right) - N_{\mathrm{KT}}\left(\alpha\right)\right|\ , \tag{5.1}$$

and expressed it in units of $\sigma\left(\alpha\right) \equiv \sqrt{N_{\mathrm{KT}}\left(\alpha\right)}$, i.e., at every point in parameter space we have measured the difference between the number of events predicted by each model, in units of the standard deviation of the KT prediction, assuming for it an uncertainty characteristic
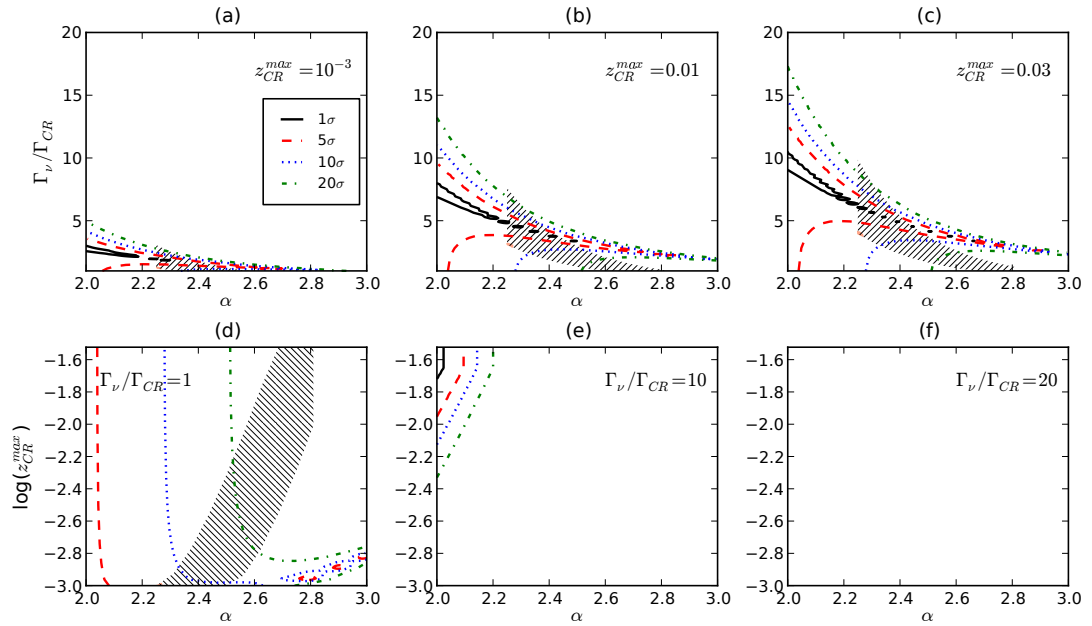
Figure 5. Same as figure 4, but assuming strong source evolution for the KT model.

of a Gaussian distribution. The higher the value of Δ, the greater the difference between the predictions. The comparison between the models, however, is only valid within the region that results from the intersection of the individual KT and BB visibility regions, given, respectively, by table 2 and figure 3. This guarantees that the numbers of events predicted by both models lie above the minimum required signal for detection at 5σ from the atmospheric neutrino background, so that the comparison between them is meaningful.

Figures 4 and 5 show the separation between the models using the integrated number of muon-neutrinos in the IceCube-86 detector. The iso-contours correspond to $\Delta/\sigma = 1$ (solid black), 5 (dashed red), 10 (dotted blue), and 20 (dash-dotted green), in the plane Γ_ν/Γ_{CR}-$-\alpha$, for values of (a) $z_{CR}^{\max} = 10^{-3}$, (b) 0.01, and (c) 0.03, and in the plane $\log(z_{CR}^{\max})$–α, for values of (d) $\Gamma_\nu/\Gamma_{CR} = 1$, (e) 10, and (f) 20. Where only one or none of the models are visible, the discrimination between them is obvious or meaningless, respectively. We have coloured orange the region of simultaneous visibility under the IC40 criterion, and hatched the region of simultaneous visibility under the AMANDA criterion. Evidently, since the individual visibility regions of the KT and BB models are larger under the AMANDA visibility criterion than under the IC40 criterion, the regions of simultaneous visibility are in every case larger under the former.

We see that the KT and BB visibility regions overlap only at low values of Γ_ν/Γ_{CR} and that the size of the overlapping regions grows with $z_{CR}^{\max}$, so that they are largest for $z_{CR}^{\max} = 0.01$ and 0.03, as shown in plots (b) and (c) of figures 4 and 5. In particular, under the AMANDA visibility criterion, and assuming no source evolution, the regions of simultaneous visibility exist only for low values of Γ_ν/Γ_{CR}, between 1 and 3, while assuming strong source evolution, they exist up to $\Gamma_\nu/\Gamma_{CR} \approx 10$. Under the IC40 visibility criterion,

– 15 –

comparison is allowed only inside very small regions of simultaneous visibility that lie at $\alpha \simeq 2.57(2.25) - 2.59(2.27)$,$\Gamma_\nu/\Gamma_{CR} \simeq 1(3) - 1.5(4)$, and $z_{CR}^{max} = 0.01 - 0.03$, assuming no (strong) source evolution. Hence, comparison between the models becomes unfeasible in most of the parameter space.

Regardless, within the small IC40 simultaneous visibility region, the models can be separated in no less than 5σ and no more than 10σ, under both assumptions on source evolution, whereas under the dated AMANDA visibility criterion separations can vary between 1σ and 20σ. Separations of 5σ would be sufficient to discern in a statistically meaningful way between the KT and BB models. Notice that the comparison at the favoured value of $\alpha = 2.7$ is not allowed under the IC40 visibility criterion, since neither flux will be visible in IceCube-86. For $\alpha = 2.0$ and 2.3, there is no region of simultaneous visibility under this same visibility criterion.

6 Summary and conclusions

We have studied the IceCube-86 event rate expectations for two models of AGN diffuse muon-neutrino flux proposed in the literature, one by Koers & Tinyakov (KT) [15] and another by Becker & Biermann (BB) [16], both of which take into account the apparent correlation, reported by the Pierre Auger Collaboration [7], between the incoming directions of the highest-energy ($E > 55$ EeV) cosmic rays and the positions of AGN in the 12th edition Véron-Cetty & Véron catalogue [9]. In doing this, we have assumed that the flux of neutrinos from AGN makes up all of the UHE astrophysical neutrino flux. Both models propose a power-law flux, i.e., proportional to $E_\nu^{-\alpha}$, resulting from shock acceleration.

In our analysis, we have taken the spectral index, α, as well as two other parameters associated to the BB model, namely, the ratio of relativistic boost factors of neutrinos and cosmic rays,Γ_ν/Γ_{CR}, and the redshift of the most distant AGN that contributes to the diffuse cosmic-ray flux, z_{CR}^{max}, as free parameters, and varied their values within the following intervals: $2 \leq \alpha \leq 3$, $1 \leq \Gamma_\nu/\Gamma_{CR} \leq 20$, and $10^{-3} \leq z_{CR}^{max} \leq 0.03$. In addition, we have explored the KT model under two assumptions on the evolution of the number density of AGN: either they do not evolve with redshift, or they evolve strongly with it, following the star formation rate. Neutrino fluxes calculated using the latter assumption are up to an order of magnitude higher than the ones calculated using the former one.

For each point $(\alpha, \Gamma_\nu/\Gamma_{CR}, z_{CR}^{max})$ in parameter space, we have calculated for both models the associated integrated number of upgoing muon-neutrinos, between 10^5 and 10^8 GeV, that is expected after five years of exposure of the full 86-string IceCube neutrino detector (IceCube-86). In order to determine the regions of parameter space that this detector will be able to probe, we have tested two different upper bounds on the UHE neutrino flux: the bound reported by the AMANDA Collaboration using 807 days of observation [38] and a preliminary bound obtained after 375 days of exposure of the half-completed IceCube-40 detector (IC40) [39]. A lower bound, on the other hand, was fixed at the estimated IceCube-86 five-year discovery potential at the 5σ level (IC86) [40]. With this we have defined "regions of visibility" in parameter space as those regions inside which the event-rate predictions lie above the IC86 discovery potential and below the AMANDA or IC40 upper bound. Since the IC40 upper bound is lower than the AMANDA bound, the former restricts the allowed parameter space more than the latter.

It is possible to confine the spectral index of the KT model within the range $2.57 \leq \alpha \leq 2.59\,(3.04)$, under the assumption of no source evolution and using the IC40 (AMANDA)

upper bound, and $2.25 \leq \alpha \leq 2.27\,(2.81)$, under the assumption of strong source evolution. For the BB model, we found that IceCube-86 is sensitive to high values of $\Gamma_\nu/\Gamma_{\rm CR}$, close to 20, only within small regions of parameter space, with $\alpha \lesssim 2.1$ and $z_{\rm CR}^{\max} \approx 0.03$. For $1 \leq \Gamma_\nu/\Gamma_{\rm CR} \lesssim 11$, under the IC40 visibility criterion, the spectral index can take on values within the interval $2 \leq \alpha \lesssim 2.65$, though the highest values are accessible only with $z_{\rm CR}^{\max} = 0.01$ to 0.03. For low values of $\Gamma_\nu/\Gamma_{\rm CR}$, around 1, the allowed ranges are $2.25 \lesssim \alpha \lesssim 2.65$ and $10^{-3} \leq z_{\rm CR}^{\max} \leq 0.03$.

Using combined cosmic-ray data [42], the preferred value of α has been set at 2.7. We have found that, if the AMANDA upper bound is used, this value is allowed in both the KT and BB models, whereas if the more recent IC40 upper bound is used, it is not. The authors of [16] claim that the true value of the spectral index might be either $\alpha = 2.0$ or 2.3. For the BB model, these two values are allowed under both visibility criteria. For the KT model, using the AMANDA bound, the value $\alpha = 2.3$ is allowed under strong source evolution, while under no source evolution it is not testable since it lies below the IC86 discovery potential. Using the IC40 bound, $\alpha = 2.3$ is excluded under strong source evolution and is also not testable under no source evolution. The value $\alpha = 2.0$ is not testable under any assumption on the source evolution. Note, however, that the experimental discovery potential and upper bounds that we have used were calculated for a E_ν^{-2} flux and that using them to constrain the BB and KT models might be slightly over-constraining the parameter space.

Additionally, in the event that an UHE neutrino signal is detected after five years of running the full IceCube array, and assuming that it was produced solely by the neutrino flux from AGN, we have explored the detector's capability to distinguish between the KT model, with strong and no source evolution, and the BB model, i.e., to determine which one of the two models would correctly describe the detected UHE neutrino data. In order to do this, we have defined a measure of the separation between the models as $\Delta\left(\alpha, \Gamma_\nu/\Gamma_{\rm CR}, z_{\rm CR}^{\max}\right) \equiv \left|N_{\rm BB}\left(\alpha, \Gamma_\nu/\Gamma_{\rm CR}, z_{\rm CR}^{\max}\right) - N_{\rm KT}\left(\alpha\right)\right|$, with $N_{\rm BB}$ and $N_{\rm KT}$ the number of muon-neutrinos expected in IceCube-86 associated to each model, between 10^5 and 10^8 GeV, after five years of running. At each point in parameter space, we have calculated the value of Δ, expressed in units of $\sigma\left(\alpha\right) \equiv \sqrt{N_{\rm KT}\left(\alpha\right)}$. The comparison between the flux models, however, is meaningful only in those regions of parameter space where both models simultaneously lie inside their respective visibility regions. Thus, under the IC40 visibility criterion, comparison is allowed only inside very small regions of simultaneous visibility located at $\alpha \simeq 2.57(2.25) - 2.59(2.27)$, $\Gamma_\nu/\Gamma_{\rm CR} \simeq 1(3) - 1.5(4)$, and $z_{\rm CR}^{\max} = 0.01 - 0.03$ assuming no (strong) source evolution. Within these regions, the separation between models is at the level of 5σ or higher. Hence, comparison between the models becomes unfeasible in most of the parameter space, but where it becomes possible, it is statistically meaningful.

A comment is in order: if, for the BB model, we had performed the integration in $z_{\rm CR}^{\max}$ up to a value ≤ 5, the associated number of events would have been larger and the corresponding visibility region even tighter than the ones we have presented, for which the contributions to the diffuse flux only come from the supergalactic plane ($z_{\rm CR}^{\max} \leq 0.03$). Since the magnitude of the separation between models relies on the number of events, then either the level of separation would have been higher or there would have been no region of simultaneous visibility.

We have thus shown that, after five years of running, the completed IceCube array might be able to strongly constrain the KT and BB models, leaving only small regions of parameter space where the models survive. In addition, discrimination between the models, while feasible only within even smaller regions of parameter space, might be able to reach

the 5σ level. The reader should be aware that our predictions are based on an all-proton cosmic-ray flux, but there is growing evidence that the UHECR flux is composed mainly of heavy nuclei [49–52] (see, however, [53, 54]), and, as a consequence, the UHE neutrino flux would be reduced. Thus, with reservations, our results might be seen as symptoms of the need for new models of AGN neutrino production that are better equipped to face the latest experimental bounds on the UHE neutrino flux.

Acknowledgments

A   Neutrino detection in IceCube

We have calculated the predicted number of muon-neutrinos detected in IceCube-86 using the method presented in Ref. [15]. In general, the integrated number of upgoing muon-neutrinos at a Čerenkov detector due to a diffuse flux of muon-neutrinos, $\phi_{\nu_\mu}^{\mathrm{diff}}$, with energies between E_ν^{min} and E_ν^{max}, is calculated as

$$N_{\nu,\mathrm{up}} = T\Omega \int_{E_\nu^{\mathrm{min}}}^{E_\nu^{\mathrm{max}}} dE_\nu \; \phi_{\nu_\mu}^{\mathrm{diff}}(E_\nu) \, A_{\nu,\mathrm{eff}}^{\mathrm{up}}(E_\nu) \; , \tag{A.1}$$

where T is the detector's exposure time; Ω, the detector's opening solid angle; E_ν, the neutrino energy; $\phi_{\nu_\mu}^{\mathrm{diff}}$ is either the KT or BB diffuse AGN neutrino flux; and $A_{\nu,\mathrm{eff}}^{\mathrm{up}}$ is the upgoing neutrino effective area.

Note that the six extra DeepCore strings of the IceCube-86 array increase the neutrino effective area only in the range $10 \leq E_\nu/\mathrm{GeV} \leq 10^3$ [55]. Above 10^3 GeV, the IceCube effective area is determined solely by the remaining 80 strings.

The effective neutrino area takes the form

$$A_{\nu,\mathrm{eff}}^{\mathrm{up}}(E_\nu) = S(E_\nu) \, P_\mu(E_\mu) \, A_{\mu,\mathrm{eff}}(E_\mu) \; , \tag{A.2}$$

where S is the shadowing factor, which takes into account neutrino interactions within the Earth; P_μ, the probability that the neutrino-spawned muon reaches the detector with energy greater than the threshold energy E_μ^{min} required to be detected; and $A_{\mu,\mathrm{eff}}$, the detector's effective area for muons. We will explain each term in eq. (A.2) in what follows.

The probability of muon detection can be written as [15]

$$P_\mu(E_\mu) = 1 - \exp(-N_{\mathrm{Av}}\sigma_{\nu N}^{\mathrm{CC}}(E_\nu) \, R_\mu(E_\mu)) \; , \tag{A.3}$$
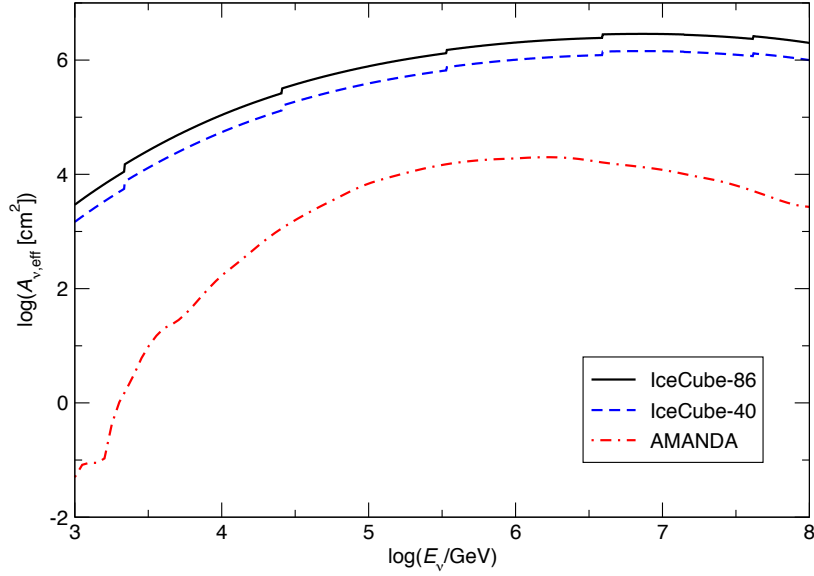
Figure 6. Angle-averaged upgoing neutrino effective areas, as functions of the neutrino energy, for the IceCube-86, IceCube-40, and AMANDA detectors. The IceCube-40 effective area is estimated at half the IceCube-86 area (see text), while the AMANDA effective area is a factor of 100 lower than the IceCube-86 area.

where $N_{\text{Av}} = 6.022 \times 10^{23} \text{ mol}^{-1} = 6.022 \times 10^{23} \text{ cm}^{-3}$ (w.e., water equivalent) is Avogadro's constant; $\sigma_{\nu N}^{\text{CC}}$ is the charged-current neutrino-nucleon cross section, taken from [56] (which uses CTEQ4 data); and R_μ is the muon range within which the muon energy reaches the threshold energy $E_\mu^{\min} = 100$ GeV, which can be expressed as

$$R_\mu\left(E_\mu\right) = \frac{1}{b} \ln \left(\frac{a + bE_\mu}{a + bE_\mu^{\min}} \right) , \tag{A.4}$$

with $a = 2.0 \times 10^{-3}$ GeV cm^{-1} (w.e.) accounting for ionisation losses and $b = 3.9 \times 10^{-6}$ cm^{-1} (w.e.) accounting for radiation losses. The relation between neutrino and muon energy is obtained by assuming single-muon production in each neutrino interaction, which leads to $E_\mu = y_{\text{CC}}\left(E_\nu\right) E_\nu$, with y_{CC} the mean charged-current inelasticity parameter tabulated in [56].

The shadowing factor, S, is defined in terms of $P_\nu\left(E_\nu, \theta\right)$, the probability that a neutrino arriving at Earth with nadir angle θ (the North Pole is located at $\theta = 0°$) and interacting with Earth matter, reaches the detector. We use [15]

$$S\left(E_\nu\right) = \frac{1}{1 - \cos\left(\theta_{\max}\right)} \int_0^{\theta_{\max}} d\theta \sin\left(\theta\right) P_\nu\left(E_\nu, \theta\right) , \tag{A.5}$$

where $\theta_{\max}$ is the detector's maximum viewing angle, which we have taken to be $\theta_{\max} = 85°$, as in Ref. [15]. Thus, the detector's opening angle is

$$\Omega = \int_0^{2\pi} d\phi \int_0^{\theta_{\max}} \sin\left(\theta\right) d\theta = 2\pi \left[1 - \cos\left(\theta_{\max}\right)\right] \approx 5.736 \text{ sr} .$$

– 19 –

The neutrino survival probability can be written as

$$P_\nu \left(E_\nu, \theta\right) = \exp\left(-N_{\mathrm{Av}}\sigma_{\nu N}^{\mathrm{tot}}\left(E_\nu\right) \int_0^{L(\theta)} \rho\left(r\right) dl\right) , \qquad (A.6)$$

where $\sigma_{\nu N}^{\mathrm{tot}}$ is the total (charged- plus neutral-current) neutrino-nucleon cross section, tabulated in Ref. [56]; $\rho\left(r\right)$ is the Earth's density profile given by the Preliminary Reference Earth Model [57], parametrised by the radial coordinate $r = \sqrt{l^2 + r_E^2 - 2lr_E\cos\left(\theta\right)}$, with $r_E = 6371$ km the Earth radius; and $L\left(\theta\right) = 2r_E\cos\left(\theta\right)$ is the distance that a neutrino traversing the Earth at angle θ propagates.

Lastly, for IceCube-86's upgoing muon effective area, $A_{\mu,\mathrm{eff}}$, we have used the curve corresponding to level-2 cuts in Figure 5 of Ref. [41], which is the effective area averaged over the northern hemisphere, and dependent only on the incoming muon energy, E_μ. Figure 6 shows that the IceCube-40 neutrino effective area is estimated at one half the IceCube-86 effective area (see Section 3), while the AMANDA neutrino effective area was a factor of 100 lower than IceCube-86 area.

References

[1] M. C. Bentz, B. M. Peterson, R. W. Pogge and M. Vestergaard, *The black hole mass-bulge luminosity relationship for active galactic nuclei from reverberation mapping and Hubble Space Telescope imaging*, Astrophys. J. Lett. **694** (2009) L166 [`arXiv:0812.2284`].

[2] J. Aird et al., *The evolution of the hard X-ray luminosity function of AGN*, Mon. Not. Roy. Astron. Soc. **401** (2010) 2531 [`arXiv:0910.1141`].

[3] B. McKernan, K. E. S. Ford and C. Reynolds, *Black hole mass, host galaxy classification and AGN activity*, [`arXiv:1005.4907`].

[4] C. M. Gaskell, *An improved [O III] line width to stellar velocity dispersion calibration: curvature, scatter, and lack of evolution in the black-hole mass versus stellar velocity dispersion relationship*, [`arXiv:0908.0328`].

[5] K. Ptitsyna and S. V. Troitsky, *Physical conditions in potential sources of ultra-high-energy cosmic rays: updated Hillas plot and radiation-loss constraints*, Phys. Usp. **53** (2010) 7 [`arXiv:0808.0367`].

[6] M. Kachelriess, *Lecture notes on high energy cosmic rays*, [`arXiv:0801.4376`].

[7] P. Abreu et al. [Pierre Auger Observatory Collaboration], *Update on the correlation of the highest energy cosmic rays with nearby extragalactic matter*, Astropart. Phys. **34** (2010) 314 [`arXiv:1009.1855`].

[8] J. Abraham et al. [Pierre Auger Collaboration], *Correlation of the highest-energy cosmic rays with the positions of nearby active galactic nuclei*, Astropart. Phys. **29** (2008) 188 [Erratum-*ibid* 30200845] [`arXiv:0712.2843`].

[9] M. P. Véron-Cetty and P. Véron *A catalogue of quasars and active nuclei: 12th edition*, Astron. Astrophys. **455** (2006) 773.

[10] H. B. J. Koers and P. Tinyakov, *Testing large-scale (an)isotropy of ultra-high energy cosmic rays*, JCAP **0904** (2009) 003 [`arXiv:0812.0860`].

[11] G. R. Farrar, I. Zaw and A. A. Berlind, *Correlations between Ultrahigh Energy Cosmic Rays and AGNs*, [`arXiv:0904.4277`].

[12] E. Waxman and J. N. Bahcall, *High energy neutrinos from astrophysical sources: an upper bound*, Phys. Rev. **D 59** (1999) 023002 [`hep-ph/9807282`].

[13] J. N. Bahcall and E. Waxman, *High energy astrophysical neutrinos: the upper bound is robust*, Phys. Rev. **D 64** (2001) 023002 [`hep-ph/9902383`].

[14] M. Kachelriess, *Ultrahigh energy neutrinos: theoretical aspects*, J. Phys. Conf. Ser. **203** (2010) 012018.

[15] H. B. J. Koers and P. Tinyakov, *Relation between the neutrino flux from Centaurus A and the associated diffuse neutrino flux*, Phys. Rev. **D 78** (2008) 083009 [`arXiv:0802.2403`].

[16] J. K. Becker and P. L. Biermann, *Neutrinos from active black holes, sources of ultra high energy cosmic rays*, Astropart. Phys. **31** (2009) 138 [`arXiv:0805.1498`].

[17] X. W. Xu [IceCube Collaboration], *Results achieved with AMANDA*, Nucl. Phys. **175-176** (Proc. Suppl.) (2008) 401

[18] F. Halzen, *IceCube Science*, J. Phys. Conf. Ser. **171** (2009) 012014 [`arXiv:0901.4722`].

[19] M. Kachelriess and D. V. Semikoz, *Reconciling the ultra-high energy cosmic ray spectrum with Fermi shock acceleration*, Phys. Lett. **B 634** (2006) 143 [`astro-ph/0510188`].

[20] J. F. Beacom, N. F. Bell, D. Hooper, S. Pakvasa and T. J. Weiler, *Measuring flavor ratios of high-energy astrophysical neutrinos*, Phys. Rev. **D 68** (2003) 093005 [Erratum-*ibid* **72** (2005) 019901] [`hep-ph/0307025`].

[21] A. Bhattacharya, S. Choubey, R. Gandhi and A. Watanabe, *Ultra-high neutrino fluxes as a probe for non-standard physics*, JCAP **1009** (2010) 009 [`arXiv:1006.3082`].

[22] G. Barenboim and C. Quigg, *Neutrino observatories can characterize cosmic sources and neutrino properties*, Phys. Rev. **D 67** (2003) 073024 [`hep-ph/0301220`].

[23] J. L. Bazo, M. Bustamante, A. M. Gago and O. G. Miranda, *High energy astrophysical neutrino flux and modified dispersion relations*, Int. J. Mod. Phys. **A 24** (2009) 5819 [`arXiv:0907.1979`].

[24] M. Bustamante, A. M. Gago and C. Pena-Garay, *Energy-independent new physics in the flavour ratios of high-energy astrophysical neutrinos*, JHEP **1004** (2010) 066 [`arXiv:1001.4878`].

[25] M. Kachelriess, S. Ostapchenko and R. Tomas, *High energy radiation from Centaurus A*, New J. Phys. **11** (2009) 065017 [`arXiv:0805.2608`].

[26] M. Kachelriess, S. Ostapchenko and R. Tomas, *Multi-messenger astronomy with Centaurus A*, Int. J. Mod. Phys. **D 18** (2009) 1591 [`arXiv:0904.0590`].

[27] B. J. Boyle and R. Terlevich, *The cosmological evolution of the QSO luminosity density and of the star formation rate*, [`astro-ph/9710134`].

[28] P. Sommers, *Cosmic ray anisotropy analysis with a full-sky observatory*, Astropart. Phys. **14** (2001) 271 [`astro-ph/0004016`].

[29] A. Cuoco and S. Hannestad, *Ultra-high energy neutrinos from Centaurus A and the Auger hot spot*, Phys. Rev. **D 78** (2008) 023007 [`arXiv:0712.1830`].

[30] K. Mannheim, R. J. Protheroe and J. P. Rachen, *On the cosmic ray bound for models of extragalactic neutrino production*, Phys. Rev. **D 63** (2001) 023003 [`astro-ph/9812398`].

[31] C. J. Willott, S. Rawlings, K. M. Blundell, M. Lacy and S. A. Eales, *The radio luminosity function from the low-frequency 3CRR, 6CE & 7CRS complete samples*, Mon. Not. Roy. Astron. Soc. **322** (2001) 536 [`astro-ph/0010419`].

[32] J. S. Dunlop and J. A. Peacock, *The redshift cut-off in the luminosity function of radio galaxies and quasars*, Mon. Not. Roy. Astron. Soc. **247** (1990) 19.

[33] E. Waxman and J. N. Bahcall, *High energy neutrinos from cosmological gamma-ray burst fireballs*, Phys. Rev. Lett. **78** (1997) 2292 [`astro-ph/9701231`].

[34] J. N. Bahcall and P. Meszaros, *5-GeV to 10-GeV neutrinos from gamma-ray burst fireballs*,

Phys. Rev. Lett. **85** (2000) 1362 [`hep-ph/0004019`].

[35] P. Meszaros and S. Razzaque, *Theoretical aspects of high energy neutrinos and GRB*, [`astro-ph/0605166`].

[36] R. Abbasi et al. [IceCube Collaboration], *Search for high-energy muon neutrinos from the 'naked-eye' GRB 080319B with the IceCube neutrino telescope*, *Astrophys. J.* **701** (2009) 1721 [Erratum-*ibid* **708** (2010) 911] [`arXiv:0902.0131`].

[37] J. K. Becker, private communication (2009).

[38] A. Achterberg et al. [IceCube Collaboration], *Multi-year search for a diffuse flux of muon neutrinos with AMANDA-II*, *Phys. Rev.* **D 76** (2007) 042008 [Erratum-*ibid* **77** (2008) 089904] [`arXiv:0705.1315`].

[39] S. Grullon, *Searching for high energy diffuse astrophysical muon neutrinos with IceCube*, [`arXiv:1005.4962`].

[40] S. Grullon and T. Montaruli, private communication (2010).

[41] J. Ahrens et al. [IceCube Collaboration], *Sensitivity of the IceCube detector to astrophysical sources of high energy muon neutrinos*, *Astropart. Phys.* **20** (2004) 507 [`astro-ph/0305196`].

[42] V. Berezinsky, A. Z. Gazizov and S. I. Grigorieva, *On astrophysical solution to ultra high energy cosmic rays*, *Phys. Rev.* **D 74** (2006) 043005 [`hep-ph/0204357`].

[43] M. G. Baring, *Diffusive shock acceleration of high energy cosmic rays*, *Nucl. Phys. Proc. Suppl.* **136** (2004) 198 [`astro-ph/0409303`].

[44] J. Bednarz and M. Ostrowski, *Energy spectra of cosmic rays accelerated at ultrarelativistic shock waves*, *Phys. Rev. Lett.* **80** (1998) 3911 [`astro-ph/9806181`].

[45] N. S. Kardashev, *Nonstationarity of spectra of young sources of nonthermal radio emission*, *Astronomic. Z.* **39** (1962) 393 (English translation in *Soviet Astron.* **6** (1962) 317).

[46] A. Meli, J. Becker, J. J. Quenby and J. Luenemann, *Particle acceleration in relativistic subluminal shock environments*, [`arXiv:0708.1438`].

[47] A. Meli, J. K. Becker and J. J. Quenby, *Cosmic ray acceleration in subluminal and superluminal relativistic shock environments*, *Astron. Astrophys.* **492** (2008) 323 [`arXiv:0709.3031`].

[48] C. A. Argüelles, M. Bustamante and A. M. Gago, In preparation.

[49] J. Abraham et al. [Pierre Auger Collaboration], *Studies of cosmic ray composition and air shower structure with the Pierre Auger Observatory*, [`arXiv:0906.2319`].

[50] D. Hooper and A. M. Taylor, *On the heavy chemical composition of the Ultra-High Energy Cosmic Rays*, *Astropart. Phys.* **33** (2010) 151 [`arXiv:0910.1842`].

[51] J. Abraham et al. [Pierre Auger Collaboration], *Measurement of the depth of maximum of extensive air showers above 10^{18} eV*, *Phys. Rev. Lett.* **104** (2010) 091101 [`arXiv:1002.0699`].

[52] J. Abraham et al. [Pierre Auger Collaboration], *Measurement of the energy spectrum of cosmic rays above 10^{18} eV using the Pierre Auger Observatory*, *Phys. Lett.* **B 685** (2010) 239 [`arXiv:1002.1975`].

[53] R. U. Abbasi et al. [HiRes Collaboration], *Indications of proton-dominated cosmic ray composition above 1.6 EeV*, *Phys. Rev. Lett.* **104** (2010) 161101 [`arXiv:0910.4184`].

[54] G. Wilk and Z. Wlodarczyk, *On the chemical composition of cosmic rays of highest energy*, [`arXiv:1006.1781`].

[55] C. Wiebusch [IceCube Collaboration], *Physics capabilities of the IceCube DeepCore detector*, [`arXiv:0907.2263`].

[56] R. Gandhi, C. Quigg, M. H. Reno and I. Sarcevic, *Neutrino interactions at ultrahigh energies*,

Phys. Rev. **D 58** (1998) 093009 [`hep-ph/9807264`].

[57] R. Gandhi, C. Quigg, M. H. Reno and I. Sarcevic, *Ultrahigh-energy neutrino interactions,* *Astropart. Phys.* **5** (1996) 81 [`hep-ph/9512364`].

Searching for cavities of various densities in the Earth's crust with a low-energy $\bar{\nu}_e$ β-beam

C.A. Argüelles[1,2],[*] M. Bustamante[1],[†] and A.M. Gago[1][‡]

[1]*Sección Física, Departamento de Ciencias, Pontificia Universidad Católica del Perú, Apartado 1761, Lima, Perú and*
[2]*Fermilab, Theoretical Physics Department, P.O. Box 500, Batavia, IL 60510, USA*

(Dated: January 31, 2012)

We propose searching for deep underground cavities of different densities in the Earth's crust using a long-baseline $\bar{\nu}_e$ disappearance experiment, realised through a low-energy β-beam with highly enhanced luminosity. We focus on four real-world cases: water-filled cavities, iron-banded formations, heavier mineral deposits, and regions of abnormal charge accumulation that, supposedly, appear prior to the occurrence of an intense earthquake. The sensitivity to identify cavities attains confidence levels higher than 3σ and 5σ for exposures times of 3 months and 1.5 years, respectively, and cavity densities below 1 g cm^{-3} or above 5 g cm^{-3}, with widths greater than 200 km. We reconstruct the cavity density, width, and position, assuming one of them known while keeping the other two free, in each of the aforementioned cases. Finally, we introduce an observable to quantify the presence of a cavity by changing the orientation of the $\bar{\nu}_e$ beam.

Introduction.– Experiments performed during the last decade have confirmed that neutrinos can change flavour with a probability that depends on neutrino energy, distance travelled, squared-mass differences $\Delta m_{21}^2 \equiv m_2^2 - m_1^2$ and $\Delta m_{31}^2 \equiv m_3^2 - m_1^2$, a CP-violation phase δ, and on the mixing angles θ_{12}, θ_{23} and θ_{13} that describe the rotation between the mass and flavour eigenstates. In the presence of matter, coherent forward scattering modifies the mass-squared differences and angles, and so the value of this probability is altered [1, 2].

In this letter, we have used neutrino oscillations in matter to discover regions of under– and over–density compared to the average density of the Earth's crust. This has already been discussed in the literature, in the context of petroleum-filled cavities, employing either a superbeam [3] or the flux of ^{7}Be solar neutrinos [4], and of electric charge accumulation in seismic faults prior to earthquakes [5], employing reactor neutrinos. In contrast, we have kept the cavity density as a free parameter, and studied how different values affect our ability to locate the cavity and to determine its density. Our experimental arrangement considers long-baseline (1500 km) neutrino disappearance using a low-energy (5–150 MeV) β-beam, which provides a high-purity sample of $\bar{\nu}_e$ and allows for intense matter effects.

Neutrino propagation in matter.– The probability amplitudes for the transitions $\bar{\nu}_e \rightarrow \bar{\nu}_\beta$ can be arranged in a column vector $\Psi_e = (\psi_{ee}\ \psi_{e\mu}\ \psi_{e\tau})^T$ which evolves according to $id\Psi_e/dx = H\Psi_e$, where x is the distance travelled since creation and the effective Hamiltonian in the flavour basis is given by $H(x) = 1/(2E_\nu)U^\dagger\text{diag}(0, \Delta m_{21}^2, \Delta m_{31}^2)U + A(x)$, with E_ν the

[*] c.arguelles@pucp.edu.pe
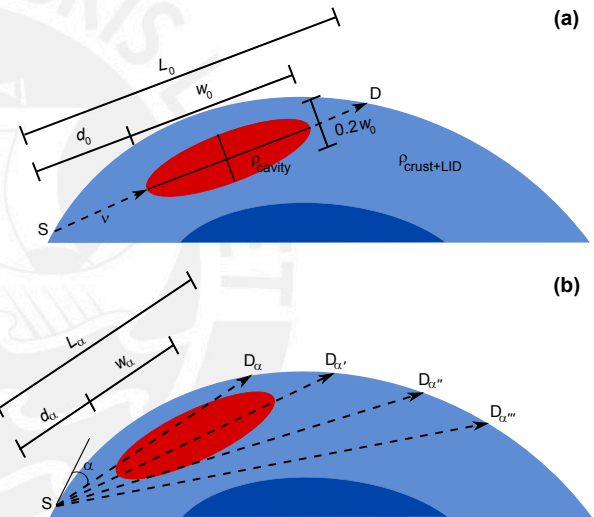[†] mbustamante@pucp.edu.pe
[‡] agago@pucp.edu.pe

FIG. 1: (Color online) Cavity and neutrino beam with a fixed (a) and different orientations (b).

neutrino energy and U the lepton mixing matrix [6]. The matter effects are encoded in the matrix $A(x) = \text{diag}(-\sqrt{2}G_F N_e(x), 0, 0)$, where $N_e(x) = y_e\rho(x)N_{\text{Av}}$ is the electron number density, with ρ the matter density, N_{Av} Avogadro's number, and $y_e = 0.494$ in the crust [5]. We have assumed a normal mass hierarchy ($\Delta m_{32}^2 > 0$), fixed the values of the squared-mass differences and angles to the best-fit values of Ref. [7], and the CP phase to zero. Our results are obtained by solving numerically the evolution equation described above.

For a qualitative understanding, we will use for the flavour-transition probability the well-known [8] formula $P_{\bar{\nu}_e \rightarrow \bar{\nu}_e}^{3\nu} = P_{\bar{\nu}_e \rightarrow \bar{\nu}_e}^{2\nu}\cos^4\theta_{13} + \sin^4\theta_{13}$ (with $A \rightarrow A\cos^2\theta_{13}$), where $P_{\bar{\nu}_e \rightarrow \bar{\nu}_e}^{2\nu}$ is the two-flavour slab approximation, valid on a piecewise constant density pro-

file [9], in the three-layer case that will be pertinent to this work. It is described by $P^{2\nu}_{\bar{\nu}_e \to \bar{\nu}_e} = |[\mathcal{U}]_{11}|^2$, where $\mathcal{U} = \mathcal{U}_3 \times \mathcal{U}_2 \times \mathcal{U}_1$, $\mathcal{U}_k = \cos\phi_k - i(\vec{n}_k \cdot \vec{\sigma})\sin\phi_k$, $\vec{\sigma}$ is the vector of Pauli matrices, and $\vec{n}_k = (\sin 2\theta_{M_k}, 0, -\cos 2\theta_{M_k})$, with θ_{M_k} the matter mixing angle in the k-th slab. The frequencies ϕ_k are given by $\Delta m^2_{M_k} x_k/(4E_\nu)$, where x_k is the width of the k-th slab, and $\Delta m^2_{M_k}$ is the squared-mass difference. The numerical calculation and this approximation are in reasonable agreement when using for the latter the dominant oscillation parameters Δm^2_{21} and θ_{12}.

Location and shape of the cavity inside the Earth.– We have assumed the existence of a cavity of uniform density ρ_{cavity} located within the Earth's crust, itself of density given by the Preliminary Reference Earth Model (PREM) [10]. Together, the ocean, crust, and LID layers of the PREM have a depth of up to 80 km and an average density of $\langle\rho_\oplus\rangle = 3.3$ g cm^{-3}. Interesting geological features such as porous rock cavities, mineral deposits and seismic faults lie in the crust and LID layers. Therefore, we have supposed that no part of the cavity is below 80 km. The cavity itself has been modelled as an ellipsoid, and we have studied an elliptic cross section of it, with major axis length w_0 and minor axis length $0.2w_0$, as shown in Fig. 1a.

Since the density profile of the Earth is radially symmetric, the position of the neutrino source (S) can be fixed at an arbitrary point on its surface, for a given source-detector baseline, L_0. In order to specify the location of the cavity, we need to set the distance d_0 measured along the baseline from the source to the cavity's surface.

Low-energy β-beams.– There is currently a proposal to use a pure, collimated beam of low-energy $\bar{\nu}_e$ generated by means of the well-understood β decay of boosted exotic ions [11] and detected through $\bar{\nu}_e + {}^{12}\text{C} \to e^+ + {}^{12}\text{B}$ [12]. Our β-beam setup contemplates an ion storage ring of total length $l_{\text{tot}} = 1885$ m, with two straight sections of length $l_{\text{straight}} = 678$ m each [13]. Inside the ring, ^{6}He ions boosted up to a Lorentz factor $\gamma = 25$ decay through $^6_2\text{He}^{++} \to {}^6_3\text{Li}^{+++} + e^- + \bar{\nu}_e$ with a half-life $t_{1/2} = 0.8067$ s. Ion production with an ISOLDE technique [14] is expected to provide a rate of ion injection of $g = 2 \times 10^{13}$ s^{-1} for ^{6}He; we have assumed a highly optimistic 5000-fold enhancement of this value, which has not even been considered in the literature.

The neutrino flux from the β decay of a nucleus in its rest frame is given by the formula [15] $\Phi_{\text{c.m.}}(E_\nu) = bE_\nu^2 E_e \sqrt{E_e^2 - m_e^2} F(\pm Z, E_e) \Theta(E_e - m_e)$, where $b = \ln 2/(m_e^5 f t_{1/2})$, with m_e the electron mass and $ft_{1/2} = 806.7$ the comparative half-life. The energy of the emitted electron is given by $E_e = Q - E_\nu$, with $Q = 3.5078$ MeV the Q-value of the reaction, and $F(\pm Z, E_e)$ the Fermi function.

Based on the formalism of Ref. [16], we have considered a cylindrical detector made of carbon, of radius $R = 4\sqrt{5}$ m and length $h = 100$ m, co-axial to the straight sections of the storage ring, and located at a distance $L_0 = 1500$
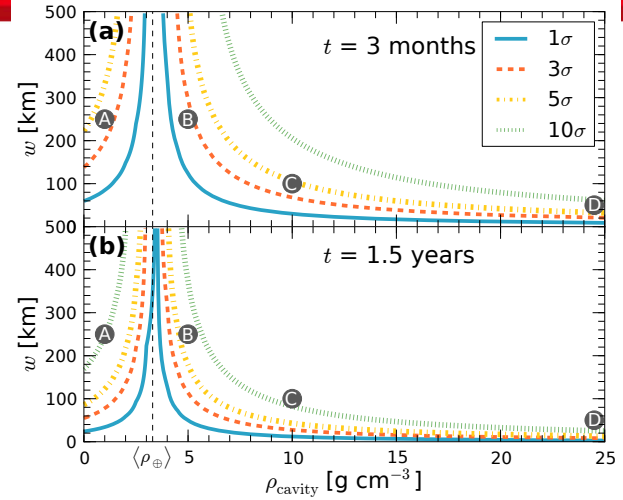

FIG. 2: (Color online) Confidence levels (C.L.s) in the w vs. ρ_{cavity} plane assuming there is no cavity. The four points A–D are special cases described in the text.

km from it. The integrated number of e^+ at the detector, after an exposure time t, is calculated as

$$N = tg\frac{t_{1/2}}{\ln 2}nh \int dE_\nu \Phi_{\text{tot}}(E_\nu) P_{\bar{\nu}_e \to \bar{\nu}_e}(L_0, E_\nu) \sigma(E_\nu) \ ,$$
(1)

with $n \approx 6.03 \times 10^{23}$ cm^{-3} the density of carbon nuclei in the detector and σ the detection cross section [12]. Since $L_0 \gg l_{\text{tot}}, l_{\text{straight}}, h$, we can write $\Phi_{\text{tot}}(E_\nu) \simeq \Phi_{\text{lab}}(E_\nu, \theta = 0)(l_{\text{straight}}/l_{\text{tot}}) S/(4\pi L_0^2)$, where Φ_{lab} is the flux in the laboratory frame [15], θ is the angle of emission of the neutrino with respect to the beam axis, and $S = \pi R^2$ is the detector's transverse area.

Sensitivity to cavities.– Assuming that there is no cavity along the baseline L_0, we evaluate the sensitivity to differentiate this situation from the hypothesis that the neutrino beam traverses a cavity of width w, position d, and density ρ. To do this, we define

$$\chi^2(w, d, \rho) = \sum_i \frac{[N_i^{\text{cav}}(w, d, \rho) - N_i^{\text{no-cav}}]^2}{N_i^{\text{no-cav}}} \ ,$$
(2)

with $N_i^{\text{cav}}(w, d, \rho)$ the number of e^+, in the i-th energy bin, that reach the detector in the case where the beam traverses the cavity, and $N_i^{\text{no-cav}}$ the corresponding number in the no-cavity case. Given that $\gamma = 25$, the neutrino spectrum extends from 5 to 150 MeV, in bins of 5 MeV. On account of the maximum energy considered, the production of muons, from $\bar{\nu}_\mu + {}^{12}\text{C} \to \mu^+ + X$, is inhibited, and thus the $\bar{\nu}_e \to \bar{\nu}_\mu$ channel is not included in this work.

Before presenting the results, it is convenient to mention that, within the slab approximation, the first and third slabs correspond to the crust, and the second one, to the cavity, so that $x_1 = d$, $x_2 = w$, and $x_3 = L_0 - d - w$.

TABLE I: Minimum value of ρ_{cavity} to have a statistical significance of 5σ or 10σ C.L. with respect to the no-cavity case, for a given width w and exposures of 3 months or 1.5 years.

| Cavity width (w) | $\rho_{\text{cavity}}[\text{g cm}^{-3}]$ | | | |
| | 3 months | | 1.5 years | |
	5σ	10σ	5σ	10σ
50 km	18	> 25	9	15
100 km	10	18	6	9
250 km	6.5	9	4.5	6

FIG. 3: (Color online) Confidence levels in the w vs. ρ plane. Plots (a)–(d) correspond to central cavities A–D from Fig. 2. The real values (ρ_0, w_0) are marked by crosses and the best-fit values by stars.

Fig. 2 shows the sensitivity in the form of isocontours of $\chi^2 = 1\sigma$, 3σ, 5σ, and 10σ, with the cavity located at the center of the baseline, so that $d = (L_0 - w)/2$ (which is tantamount to $\phi_1 = \phi_3$), and detector exposure times of (a) 3 months and (b) 1.5 years. Because of this relation between d and w, the analysis can be reduced to two parameters: ρ and w (or d). It is observed that the sensitivity improves as $|\rho_{\text{cavity}} - \langle\rho_\oplus\rangle|$ increases. Also, the statistical significance, for the cavity hypothesis, grows with w, given that the cumulative matter density differences are greater.

In the slab approximation, the behaviour of the oscillation probability, that dictates the shape of the isocontours, is dominated by the ϕ_2 frequency, which is the only one that depends on both ρ and w. In fact, for a given energy, and since we have observed that the combinations of sines and cosines of ϕ_1 in the probability vary slowly with w, each isocontour approximately corresponds to a constant value of $w\sqrt{c_0^2/E_\nu^2 + 2c_0c_1\rho\cos 2\theta_{12}/E_\nu + c_1^2\rho^2}$, where $c_0 = \Delta m_{21}^2/4$ and $c_1 = -G_F y_e N_{\text{Av}}\cos^2\theta_{13}/\sqrt{2}$. Table I shows the minimum value of ρ_{cavity} needed to reach 5σ and 10σ separations, for small ($w = 50$ km), medium (100 km), and large (250 km) cavities, after detector exposure times of 3 months and 1.5 years.

Determination of cavity parameters.– The next step in the analysis is to change the assumption of no-cavity to that of a real cavity. This implies replacing $N_i^{\text{no-cav}} \rightarrow N_i^{\text{cav}}(w_0, d_0, \rho_{\text{cavity}})$ in Eq. (2). Firstly, we consider a known cavity position (i.e., $d = d_0$, with the hypothetical cavity no longer centered) and, heretofore, we set 1.5 years as exposure time, unless otherwise specified, and keep the other details of the study equal to those presented in the sensitivity analysis. We will study the four points, motivated by centered real-world cavities, marked in Fig. 2: A ($\rho_{\text{cavity}} = 1$ g cm^{-3}, $y_e = 0.555$, $w_0 = 250$ km), corresponding to a deep water-filled underground cavity, B ($\rho_{\text{cavity}} = 5$ g cm^{-3}, $y_e = 0.5$, $w_0 = 250$ km), to an iron banded formation [17], C ($\rho_{\text{cavity}} = 10$ g cm^{-3}, $y_e = 0.5$, $w_0 = 100$ km), to a heavier mineral deposit, and D ($\rho_{\text{cavity}} = 25$ g cm^{-3}, $y_e = 0.5$, $w_0 = 50$ km), representing a zone of seismic faults with the typical charge accumulation that supposedly exists prior to an earthquake of magnitude 7 in the Richter scale [18]. In Ref. [5],
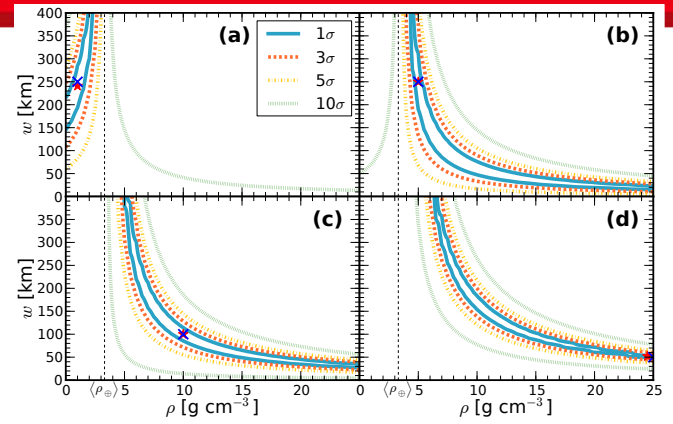
a value of $\rho_{\text{cavity}} \approx \langle\rho_\oplus\rangle$ and a maximum value of $y_e \approx 4$ at the fault are used, while, to keep in line with the analysis of cavities A–C, we have equivalently taken for cavity D $\rho_{\text{cavity}} = 25$ g cm^{-3} and $y_e = 0.5$.

Notice that the closest distance from the cavities to the Earth surface, for A and B, is about 19 km, and, for cavities C and D, 34 km and 39 km, respectively. Wider or uncentered cavities would lie closer to the surface; for instance, a centered cavity with $w_0 = 323$ km would lie only 12 km deep, which is roughly the current maximum drilling depth [19].

Secondly, in Fig. 3 we observe that values of ρ close to $\langle\rho_\oplus\rangle$ (equivalent to the no-cavity case), regardless of w, are excluded at the same statistical significance as shown in Fig. 2. The shape of the isocontours is explained by the same argument as in said figure. The uncertainty in w is large in cases A and B, since in that density region the contours are parallel to the asymptote at $\rho = \langle\rho_\oplus\rangle$. In cases C and D, the uncertainty is smaller given that at higher densities the contour regions tend to be parallel to the horizontal axis. It is interesting to point out that in a real-case scenario, where there could be some prior knowledge about the density, it would be possible to constrain w significantly. For instance, for $\rho = 1$ g cm^{-3} (case A), $w = 240^{+30}_{-50}$ km at 1σ uncertainties, while for $\rho = 25$ g cm^{-3} (case D), $w = 50 \pm 10$ km.

In Fig. 4, we display the case where the cavity position is unknown, while its density is known (i.e., $\rho = \rho_{\text{cavity}}$) and, thus, the contour regions are described by w and d (with $w + d \leq L_0$). In this figure, the size of the uncertainty in w follows from Fig. 3. Therefore, we are capable of determining w with reasonable precision in cases C and D. On the other hand, the determination of d improves mildly as the density increases. For example, in case A, $d = 600^{+375}_{-475}$ km and, in D, $d = 725^{+225}_{-275}$ km at 1σ uncertainties. Using the slab approximation, this larger uncertainty can be explained by the weak dependence of
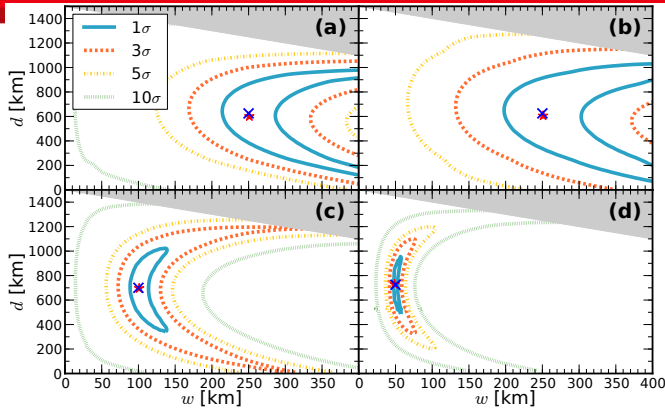
FIG. 4: (Color online) Confidence levels in the d vs. w plane. Plots (a)–(d) correspond to central cavities A–D from Fig. 2. The real values (w_0, d_0) are marked by crosses and the best-fit values by stars.
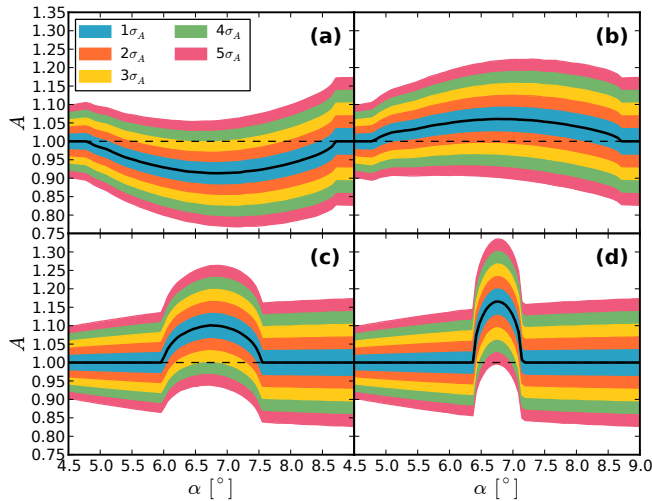

FIG. 5: (Color online) In solid black lines, A vs. α, for the four cavities A–D, together with selected uncertainty regions.

the probability, for most of the relevant energy range, on ϕ_1 and ϕ_3, and, therefore, on d.

Searching for a cavity.– We have explored the possibility of varying the beam orientation, defined by the angle α measured with respect to the tangent to Earth at S, as a way of finding a cavity. This is shown in Fig. 1b, and could be implemented by using a mobile neutrino detector, either on land or at sea [20]. At an angle α, the beam travels a baseline L_α; for some values, it will cross a portion of the cavity with position d_α and width w_α. To quantify the size of the traversed portion, we have defined

$$A(L_0, w_0, d_0, \alpha, \rho_{\text{cavity}}) = \frac{N^{\text{cav}}(L_\alpha, w_\alpha, d_\alpha, \rho_{\text{cavity}})}{N^{\text{no-cav}}(L_\alpha)}, \tag{3}$$

with N^{cav} and $N^{\text{no-cav}}$ the total numbers of e^+ between 5 and 150 MeV, and L_α, w_α, d_α functions of L_0, w_0, d_0, and α. For this analysis, we have set the exposure time at $t = 3$ months.

Fig. 5 shows the A vs. α curves for the four cavities A–D. The curve for cavity A lies below $A = 1$ because its density is lower than $\langle\rho_\oplus\rangle$, while the densities of cavities B–D are higher. The $1\sigma_A$ to $5\sigma_A$ uncertainty regions around the curves are included, with $\sigma_A \equiv A\sqrt{(1/N^{\text{cav}})(1+A)}$ the standard deviation of A. Since $N^{\text{cav}} \sim 1/L_\alpha^2$, then $\sigma_A \sim L_\alpha$ and, given that, by geometrical construction, L_α grows with α, this means that σ_A also grows with α, a feature that is observed in Fig. 5. Similarly to previous figures, the separation from $A = 1$ grows as ρ_{cavity} moves away from $\langle\rho_\oplus\rangle$. The C.L. achieved at the maximum deviation point is not as high as those shown in Fig. 2, due to the fact the analysis of A does not take into account the spectral shape, but only the total e^+ count.

Separation from $A = 1$ at the $2\sigma_A$ C.L. is achieved for all cavities, with A and C reaching $3\sigma_A$, and D, $5\sigma_A$. Thus, the parameter A could be used as a quick estimator of the presence of a cavity, while a more detailed analysis, similar to the one performed for Fig. 4, could be used to estimate the cavity shape, i.e., its position and width, and, from the latter, its volume.

Conclusions.– We studied the use of a low-energy (5–150 MeV) β-beam of $\bar{\nu}_e$, with a baseline of 1500 km and a large luminosity enhancement, to find the presence of deep underground cavities in the Earth's crust. We have determined the sensitivity as a function of the cavity density ρ and size w (dimension of the cavity aligned with the neutrino beamline), which reaches significances in the order of 5σ (3σ) for baseline-centered cavities with densities lower than 1 g cm^{-3} or greater than 5 g cm^{-3}, exposure time of 1.5 years (3 months), and w greater than 200 km, rendering our analysis highly competitive. We analysed the C.L. regions of the reconstructed parameters of four real-world cavities in the ρ vs. w plane, for a known cavity position d, and also in the w vs. d plane, when ρ is known. Finally, we have considered sweeping the Earth in search of a cavity using an orientable neutrino beam, which proves to be a useful tool to detect its presence.

[1] M. Fukugita and T. Yanagida, *Physics of neutrinos and applications to astrophysics*, (Springer, New York, 2003).

[2] M. C. Gonzalez-Garcia and Y. Nir, Rev. Mod. Phys. **75**, 345 (2003) [hep-ph/0202058].

[3] T. Ohlsson and W. Winter, Europhys. Lett. **60**, 34 (2002) [hep-ph/0111247].

[4] A. N. Ioannisian and A. Y. Smirnov, [hep-ph/0201012].

[5] B. Wang, Y. Z. Chen and X. Q. Li, Chin. Phys. C **35**, 325 (2011) [arXiv:1001.2866].

[6] K. Nakamura *et al.* [Particle Data Group], J. Phys. G **37**, 075021 (2010).

[7] T. Schwetz, M. Tortola, J. W. F. Valle, New J. Phys. **13**, 063004 (2011) [arXiv:1103.0734].

[8] O. L. G. Peres and A. Y. Smirnov, Phys. Rev. D **79**, 113002 (2009) [arXiv:0903.5323].

[9] E. K. Akhmedov, Nucl. Phys. B **538**, 25 (1999) [hep-ph/9805272].

[10] A. M. Dziewonski and D. L. Anderson, Phys. Earth Planet. Interiors **25**, 297 (1981).

[11] C. Volpe, J. Phys. G G **34**, R1 (2007) [hep-ph/0605033].

[12] A. R. Samana, F. Krmpotic, N. Paar and C. A. Bertulani, Phys. Rev. C **83**, 024303 (2011) [arXiv:1005.2134].

[13] A. B. Balantekin, J. H. de Jesus and C. Volpe, Phys. Lett. B **634**, 180 (2006) [hep-ph/0512310].

[14] B. Autin *et al.*, J. Phys. G **29**, 1785 (2003) [physics/0306106].

[15] K. S. Krane, *Introductory nuclear physics* (Wiley, New York, 1998).

[16] J. Serreau and C. Volpe, Phys. Rev. C **70**, 055502 (2004) [hep-ph/0403293].

[17] G. B. Morey, in *Iron-formation: facts and problems*, edited by A. F. Trendall and R. C. Morris in Developments in Precambrian Geology Vol. 6 (Elsevier, Amsterdam, 1983).

[18] S. Pulinets, TAO, **15**, 3 (2004).

[19] K. Fuchs, E. A. Kozlovsky, A. I. Krivtsov and M. D. Zoback, *Super-deep continental drilling and deep geophysical sounding* (Springer, Berlin, 1990).

[20] P. Huber, Phys. Lett. B **692**, 268 (2010) [arXiv:0909.4554].

FERMILAB-PUB-12-038-T

Sterile neutrinos and indirect dark matter searches in IceCube

Carlos A. Argüelles[1,2*] and Joachim Kopp[2†]

[1]*Sección Física, Departamento de Ciencias,*
Pontificia Universidad Católica del Perú, Apartado 1761, Lima, Peru and

[2]*Fermilab, Theoretical Physics Department, PO Box 500, Batavia, IL 60510, USA*
(Dated: March 27, 2012)

If light sterile neutrinos exist and mix with the active neutrino flavors, this mixing will affect the propagation of high-energy neutrinos from dark matter annihilation in the Sun. In particular, new Mikheyev-Smirnov-Wolfenstein resonances can occur, leading to almost complete conversion of some active neutrino flavors into sterile states. We demonstrate how this can weaken IceCube limits on neutrino capture and annihilation in the Sun and how potential future conflicts between IceCube constraints and direct detection or collider data might be resolved by invoking sterile neutrinos. We also point out that, if the dark matter–nucleon scattering cross section and the allowed annihilation channels are precisely measured in direct detection and collider experiments in the future, IceCube can be used to constrain sterile neutrino models using neutrinos from the dark matter annihilation.

I. INTRODUCTION

The hunt for dark matter is currently at a very exciting, but also somewhat confusing stage. Many unexpected experimental results that have been reported over the past few years can be interpreted in terms of dark matter, but all of them could have more mundane explanations, and moreover the dark matter interpretations of different experimental data sets do not fit together in many cases. For instance, the signals reported by CoGeNT [1, 2], DAMA [3, 4] and CRESST [5] appear to be in some tension with the null results from other direct detection experiment, in particular CDMS [6, 7] and XENON-100 [8] (see, however, [9, 10]). Moreover, the dark matter parameter regions favored by CoGeNT, DAMA and CRESST do not coincide under standard assumptions on the dark matter halo [11–16] (see, however, refs. [17–20]). Also, if the recently observed anomalies in the cosmic electron and positron spectra [21, 22]) are due to dark matter annihilation or decay, this would imply dark matter masses of order 1 TeV (see, for instance, [23]), whereas the CoGeNT, DAMA and CRESST hints would indicate dark matter masses of order 10 GeV. It is thus clear that many of the potential hints for dark matter must have other explanations, and this illustrates that a single experiment might never be able to unambiguously identify dark matter. Only matching detections by several different experiments would convince the community at large that dark matter has been observed. Fortunately, the toolbox for dark matter search is quite large: Direct detection experiments like CoGeNT, DAMA, CRESST, CDMS and XENON-100 search for dark matter recoils on atomic nuclei; collider searches at the Tevatron and the LHC aim to directly produce dark matter particles and detect them through missing energy signatures; indirect searches look for the annihilation or decay products of astrophysical dark matter. Among the possible messengers are electrons and positrons, anti-protons, gamma rays, and neutrinos.

A special role is played by searches for neutrinos from dark matter annihilation in the Sun,

---

[*]Electronic address: c.arguelles@pucp.edu.pe
[†]Electronic address: jkopp@fnal.gov

which are carried out by the Super-Kamiokande [24, 25] and IceCube [26, 27] collaborations. Even though these searches probe the products of dark matter annihilation, the expected event rates are usually determined by the dark matter capture rate in the Sun and thus by the dark matter–nucleus scattering cross section. Therefore, these searches, even though indirect, are sensitive to the same observables as direct detection experiments and can directly test any potential direct detection signal (provided that dark matter can annihilate and that its annihilation products include neutrinos). In particular, many astrophysical uncertainties, for instance those associated with the local dark matter density, affect the Super-Kamiokande and IceCube searches in the same way as the direct searches, making the comparison between those experiments quite robust with respect to astrophysics.

On the other hand, neutrinos from dark matter annihilation in the Sun are strongly affected by neutrino oscillation physics. In this paper, we will investigate how the oscillations pattern of high-energy neutrinos from dark matter annihilation in the Sun can be modified by the existence of sterile neutrinos. Our study is motivated by the results of the LSND [28] and MiniBooNE [29] experiments, as well as the reactor antineutrino anomaly [30–32], all of which can be interpreted as hints for the existence of sterile neutrinos with masses of order 1 eV [33–35]. (Note, however, that even models with two sterile neutrinos cannot resolve all tension in the global data set.) We will argue that, if sterile neutrinos exist, neutrinos from dark matter annihilation can encounter new Mikheyev-Smirnov-Wolfenstein (MSW) resonances when propagating out of the Sun, and that these resonances can potentially convert a large fraction of them into undetectable sterile states. This can weaken constraints on dark matter annihilation in the Sun significantly. (The existence of new MSW resonances in the presence of sterile neutrinos has also been investigated recently in the context of IceCube atmospheric neutrino data [36, 37].) On the positive side, if the dark matter–nucleon scattering cross section and the dark matter annihilation channels are precisely determined elsewhere, for instance in direct detection and collider experiments, IceCube can be used as a sensitive tool for constraining sterile neutrino models.

The outline of the paper is as follows: In section II, we review the relevant aspects of the formalism of neutrino oscillations and discuss the effect of MSW resonances on the oscillation probabilities of high-energy neutrinos in the Sun. We then describe in section III how we compute the expected neutrino signal from dark matter annihilation in the IceCube detector, and in section IV we show how the existence of sterile neutrinos modifies the dark matter constraints from IceCube. We will discuss our results and conclude in section VI.

II. NEUTRINO OSCILLATIONS AND NEUTRINO INTERACTIONS IN THE SUN

Neutrinos from dark matter annihilation in the Sun probe a very unique regime of neutrino oscillations: They are produced in a region of very high matter density (~ 150 g/cm^3) at the center of the Sun [38], but with energies that can be much higher than those at which neutrino oscillations in the Sun are usually studied.

In the standard three-flavor oscillation framework, it is well known from the study of low-energy ($\mathcal{O}(\text{MeV})$) solar neutrinos that strong transitions between electron neutrinos, ν_e, and muon/tau neutrinos, ν_μ, ν_τ, take place in a region where the number density of electrons N_e reaches a critical value, given by the Mikheyev-Smirnov-Wolfenstein (MSW) resonance condition [39–42]

$$N_e^{\text{low}} = a_{\text{CP}} \cos\theta_{12} \frac{\Delta m_{21}^2}{2E} \frac{1}{\sqrt{2}G_F} . \tag{1}$$

Here, E is the neutrino energy, G_F is the Fermi constant, θ_{12} and Δm_{21}^2 are the usual solar neutrino mixing parameters, and $a_{\text{CP}} = 1 \, (-1)$ for neutrinos (antineutrinos). The MSW resonance condition

can be understood if we recall that according to the Fermi theory of weak interactions the local matter potential due to W exchange with an electron, which is felt by electron-neutrinos but not by muon and tau neutrinos, is given by $\sqrt{2}a_{CP}G_F n_e(r)$, with $n_e(r) = \langle \bar{e}\gamma^0 e \rangle$ the electron number density at a distance r from the center of the Sun. At high matter density near the center, the flavor-diagonal MSW potential is larger than the flavor-off-diagonal neutrino mass term $\Delta m_{21}^2/2E$ for multi-MeV neutrinos. Thus mixing between ν_e and ν_μ, ν_τ is suppressed, and mass and flavor eigenstate almost coincide. For instance, the flavor eigenstate ν_e is almost equal to the mass eigenstate ν_2 for multi-MeV neutrinos produced at the center of the Sun. At low matter density in the outer layers of the Sun, on the other hand, the mass terms dominate over the potential term, so that the effective mixing matrix is close to the vacuum mixing matrix, according to which ν_e is mostly composed of ν_1. If the change in the matter density is not too fast, neutrinos cannot "jump" from one mass eigenstate to another, so that a neutrino produced as an almost pure ν_2 will still be in an almost pure ν_2 state when it exits the Sun. However, its flavor composition has changed dramatically, and in fact, the ν_e admixture to ν_2 in vacuum is given $|U_{e2}|^2 \simeq \sin^2\theta_{12} \simeq 0.31$ (using the standard parameterization [42] and the current best fit values [43, 44] for the leptonic mixing matrix). Thus, almost 70% of the neutrinos are converted to ν_μ, ν_τ on their way out of the Sun. The flavor-conversion happens predominantly at the transition between the matter potential-dominated and the mass mixing-dominated regime, where the two terms are of similar magnitude. This requirement leads precisely to the condition (1).

For energies above ~ 100 MeV (not accessible with conventional solar neutrinos), a second MSW resonance appears at a higher density

$$N_e^{\text{high}} = a_{\text{CP}} \cos\theta_{13} \frac{\Delta m_{31}^2}{2E} \frac{1}{\sqrt{2}G_F}. \tag{2}$$

This second resonance leads to strong $\nu_e \leftrightarrow \nu_\mu, \nu_\tau$ transitions if $\Delta m_{31}^2 > 0$, and to strong $\bar{\nu}_e \leftrightarrow \bar{\nu}_\mu, \bar{\nu}_\tau$ transitions for $\Delta m_{31}^2 < 0$.

The requirement that the change in matter density be not too fast (see above) can be made more precise. One can show that resonant flavor transitions in the (ij)-sector cease when the *adiabaticity condition* [42]

$$\gamma_r \equiv \left(\frac{\Delta m_{ij}^2}{2E} \sin 2\theta_{ij} \right)^2 \frac{1}{|\dot{V}|_{\text{res}}} \gg 1 \tag{3}$$

is no longer fulfilled. Here, γ_r is called the adiabaticity parameter at the resonance and $|\dot{V}|_{\text{res}}$ denotes the gradient of the MSW potential $V = \sqrt{2}G_F N_e$ at the location of the resonance. Loss of adiabaticity thus occurs for small mixing angles, small Δm^2 and high energies. In the case of the resonance in the (12)-sector, which turned out to be the solution to the long-standing solar neutrino problem, we expect adiabatic transitions below ~ 10 GeV, and non-adiabatic behavior above. (Note that, if flavor transitions of solar neutrinos were non-adiabatic, an initial ν_e would leave the Sun not as a ν_2 mass eigenstate, but as a superposition of the form $U_{e1}^*|\nu_1\rangle + U_{e2}^* e^{i\phi}|\nu_2\rangle$, with the oscillation phase ϕ. After averaging over ϕ, this would lead to a ν_e survival probability given by $1 - \frac{1}{2}\sin^2 2\theta_{12}$, in conflict with the experimental data on solar neutrinos.)

The neutrino oscillation probabilities in the Sun in the standard three-flavor framework are plotted as a function of energy in figures 1 and 2 (black lines). The transition between the adiabatic and non-adiabatic regimes at energies around 10 GeV is clearly visible. At typical solar neutrino energies of few MeV, the ν_e survival probability has the expected value of $\sin^2\theta_{12} \simeq 0.3$, while in the non-adiabatic regime, it is $1 - \frac{1}{2}\sin^2 2\theta_{12} \simeq 0.6$. (Small deviations from these values can arise from the inclusion of three-flavor effects, in particular a non-zero θ_{13}.)
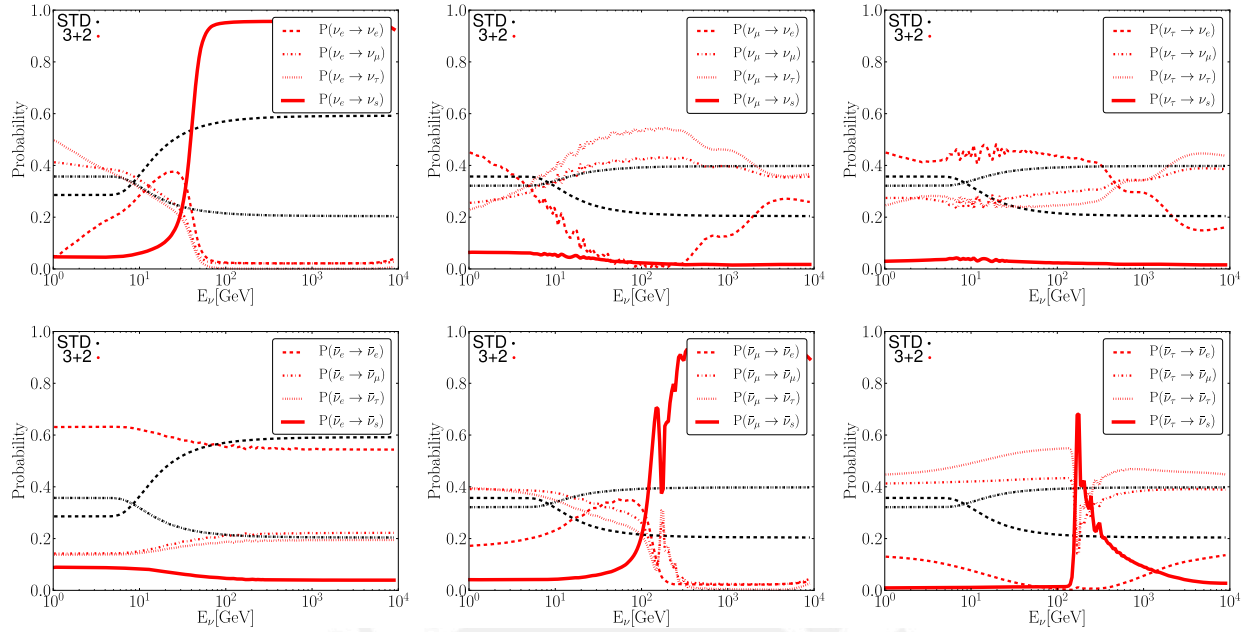
Figure 1: Flavor transition probabilities in the Sun as a function of energy for an initial ν_e (left), an initial ν_μ (center), and an initial ν_τ (right). The top plots are for neutrinos, the ones at the bottom are for anti-neutrinos. Black lines are for standard three-flavor oscillation, whereas red lines are for a representative "$3+2$" model with two sterile neutrinos (see text for details). Absorption and τ regeneration effects are neglected in these plots. Note that the black dotted lines ($\nu_x \to \nu_\tau$ in the SM) and the black dot-dashed lines ($\nu_x \to \nu_\mu$ in the SM) lie on top of each other since ν_μ–ν_τ mixing is assumed to be maximal.

If sterile neutrinos exist, the oscillation phenomenology becomes much richer. Even if *vacuum* oscillations between active and sterile neutrino flavors are negligible because of small mixing angles, active–sterile oscillations *in matter* can be significant, in particular at the high energies relevant to neutrinos from dark matter annihilation. The n-flavor MSW potential has the form

$$V = \left(n_e - n_n/2, -n_n/2, -n_n/2, 0, \dots \right),\tag{4}$$

where the terms containing the neutron density n_n originate from coherent forward scattering through Z^0 exchange. These terms are usually neglected in the three-flavor framework since they are flavor-universal and therefore cannot contribute to oscillations among active neutrinos. However, they become relevant in the presence of sterile states. In particular, there will be additional MSW resonances whenever any of the matter potential terms becomes equal to any of the mass terms in the Hamiltonian. These MSW resonance can lead to nearly complete conversion of certain neutrino (or antineutrino) flavors into sterile states on the way out of the Sun.

To illustrate this observation, which is the main topic of this paper, we consider a sterile neutrino scenario similar to the one that has been shown in Ref. [33] to provide a reasonably good fit to the global neutrino data, including the anomalous LSND and MiniBooNE results. The model has two

sterile neutrino flavors ν_{s1}, ν_{s2} and two new mass eigenstates ν_4, ν_5 with mixing parameters

$$
\begin{array}{ccc}
\sin^2\theta_{12} = 0.32 & \sin^2 2\theta_{13} = 3 \times 10^{-3} & \sin^2\theta_{23} = 0.45 \\
\Delta m_{21}^2 = 7.6 \times 10^{-5} \text{ eV}^2 & \Delta m_{31}^2 = 2.38 \times 10^{-3} \text{ eV}^2 \\
\Delta m_{41}^2 = 0.90 \text{ eV}^2 & \Delta m_{51}^2 = 0.47 \text{ eV}^2 \\
\sin^2 2\theta_{14} = 0.086 & \sin^2 2\theta_{15} = 0.060 & \sin^2 2\theta_{24} = 0.088 \\
\sin^2 2\theta_{25} = 0.055 & \sin^2 2\theta_{34} = 0.002 & \sin^2 2\theta_{35} = 0.000 \\
\delta_{13} = 1.47\pi & \delta_{14} = 1.086\pi & \delta_{15} = 0.77\pi
\end{array}
\tag{5}
$$

Here, we use the parameterization

$$
U_{3+2} = R_{45} R_{35} R_{25} R_{15}^{\delta} R_{34} R_{24} R_{14}^{\delta} R_{23} R_{13}^{\delta} R_{12}
\tag{6}
$$

for the leptonic mixing matrix, where R_{ij} denotes a rotation matrix in the (ij) plane with rotation angle θ_{ij}, and R_{ij}^{δ} denotes a similar rotation matrix which in addition carries a complex phase δ_{ij}:

$$
R_{ij} = \begin{pmatrix} \ddots & & & \\ & \cos\theta_{ij} & \cdots & \sin\theta_{ij} \\ & \vdots & & \vdots \\ & -\sin\theta_{ij} & \cdots & \cos\theta_{ij} \\ & & & & \ddots \end{pmatrix}, \qquad R_{ij}^{\delta} = \begin{pmatrix} \ddots & & & \\ & \cos\theta_{ij} & \cdots & \sin\theta_{ij} e^{-i\delta_{ij}} \\ & \vdots & & \vdots \\ & -\sin\theta_{ij} e^{i\delta_{ij}} & \cdots & \cos\theta_{ij} \\ & & & & \ddots \end{pmatrix}.
\tag{7}
$$

In a "$3+2$" scenario like equation (5), the new MSW resonances converting active neutrinos into sterile ones affect antineutrinos more strongly than neutrinos, but since neutrino cross sections are larger than antineutrino cross sections, we expect the impact of sterile neutrinos on dark matter searches to be only moderate, especially in detectors like IceCube and Super-Kamiokande which cannot distinguish neutrinos from antineutrinos. (Below, we will also discuss a $3+3$ toy model in which effects are larger.)

The neutrino oscillation probabilities in the Sun for this sterile neutrino scenario are shown in figures 1 as red curves. The most striking feature is the strong conversion of $\bar{\nu}_\mu$ (and to some degree also $\bar{\nu}_\tau$) into sterile neutrinos at energies above ~ 200 GeV. Indeed, we can see from equation 1 (with the replacements $\theta_{12} \to \theta_{14} \simeq 0, \Delta\, m_{21}^2 \to \Delta m_{41}^2 \simeq -1$ eV^2, and $N_e \to -N_n/2$) that above $E \sim 100$ GeV, the MSW resonance between active and sterile neutrinos lies within the Sun. Therefore, high energy $\bar{\nu}_\mu$ and $\bar{\nu}_\tau$ produced from dark matter annihilation at the center of the Sun will be almost fully converted into sterile neutrinos, leaving as detectable states only neutrinos, and antineutrinos from the $\bar{\nu}_e$ component of the primary flux. For a given dark matter mass, annihilation channel and annihilation cross section, the expected event number in a neutrino detector is thus reduced, so that experimental constraints on dark matter annihilation in the Sun become weaker.

In addition to the $3+2$ scenario, we are also going to consider a $3+3$ toy model with 3 sterile neutrinos. The oscillation parameters in this model are chosen such that each active neutrino flavor eigenstate mixes with only one of the sterile neutrinos. This can be achieved by choosing mass squared difference$\Delta\, m_s^2 \equiv \Delta m_{41}^2 \simeq \Delta m_{52}^2 \simeq \Delta m_{63}^2$ and mixing angles $\theta_s \equiv \theta_{14} \simeq \theta_{25} \simeq \theta_{36}$ (all other active–sterile mixing angles are zero), so that the sterile neutrino sector is a mirror image of the active neutrino sector as far as vacuum oscillations are concerned. (Similar models have been considered in [45].) The parameterization of the leptonic mixing matrix is here

$$
U_{3+3} = R_{36} R_{25} R_{14} R_{23} R_{13}^{\delta} R_{12}
\tag{8}
$$

Unless specified otherwise, we choose$\Delta m_{41}^2 = 0.1$ eV^2 and $\sin^2 2\theta_s = 0.03$. In general, ifΔm_{41}^2, Δm_{52}^2, $\Delta m_{63}^2 \gg \Delta m_{21}^2$, $|\Delta m_{31}^2|$, conversions of active neutrinos into sterile neutrinos can be understood in a simple two-flavor framework as long as the distance travelled by the neutrinos is much shorter than the active neutrino oscillation lengths $L_{21}^{\text{osc}} = 4\pi E/\Delta m_{21}^2$ and $L_{31}^{\text{osc}} = 4\pi E/|\Delta m_{31}^2|$. This remains true even in matter. In this case, the effective two-flavor oscillations between an active flavor and its corresponding sterile flavor are affected by an MSW resonance. The resonance conditions are, in analogy to equations (1) and (2):

$$N_e = a_{\text{CP}} \cos\theta_{14} \frac{\Delta m_{41}^2}{2E} \frac{1}{\sqrt{2}G_F}\,, \qquad (\nu_e \leftrightarrow \nu_{s1} \text{ transitions}) \qquad (9)$$

$$-\frac{N_n}{2} = a_{\text{CP}} \cos\theta_{25} \frac{\Delta m_{52}^2}{2E} \frac{1}{\sqrt{2}G_F}\,, \qquad (\nu_\mu \leftrightarrow \nu_{s2} \text{ transitions}) \qquad (10)$$

$$-\frac{N_n}{2} = a_{\text{CP}} \cos\theta_{36} \frac{\Delta m_{63}^2}{2E} \frac{1}{\sqrt{2}G_F}\,. \qquad (\nu_\tau \leftrightarrow \nu_{s3} \text{ transitions}) \qquad (11)$$

We see from these equations that the resonance between ν_e and the first sterile flavor eigenstate ν_{s1} will be in the neutrino sector ($a_{\text{CP}} = 1$), whereas the $\nu_\mu \leftrightarrow \nu_{s2}$ and $\nu_\tau \leftrightarrow \nu_{s3}$ resonances affect antineutrinos ($a_{\text{CP}} = -1$). This behavior is reflected in figure 2, where we show the flavor transition probabilities for all oscillation channels in the $3 + 3$ model as a function of energy. We see that in a large energy range ν_e, $\bar\nu_\mu$ and $\bar\nu_\tau$ are almost fully converted into sterile states. We expect that this will lead to a considerable weakening of the limits IceCube can set on dark matter capture and annihilation in the Sun.

Note that this weakening could be even more pronounced if the mostly active neutrino mass eigenstates were *heavier* than the mostly sterile ones, since in that case the MSW resonances for second and third generation neutrinos would move from the antineutrino sector to the neutrino sector, which is more important for IceCube's dark matter search because neutrino interaction cross sections are about a factor of 3 larger than antineutrino cross sections. We do not consider this possibility here since relatively heavy active neutrinos would be in potential conflict with cosmology [46–49]. (These conflict can potentially be avoided in non-minimal cosmologies [48, 49] and in models where the relic abundance of sterile neutrinos is reduced, see for instance references [50, 51] for a discussion of such models.)

Apart from oscillation, the propagation of high-energy neutrinos through the Sun is also affected by non-coherent neutral current (CC) and charged current (CC) interactions. NC interactions change the neutrino energy, whereas CC interactions lead to absorption and possible reemission of neutrinos in the decay of secondary μ or τ leptons. Since secondary muons are usually thermalized before they decay, reemission of *high-energy* neutrinos is only possible in the case of $\nu_\tau + X \to \tau + X'$ CC interactions ("τ regeneration"). In figure 3 we plot the non-interaction ("survival") probability for neutrinos from dark matter annihilation on their way out of the Sun as a function of the neutrino energy.

III. SIMULATION TECHNIQUES

To estimate quantitatively how existing limits on dark matter annihilation in the Sun are modified in the presence of sterile neutrinos, we have carried out numerical simulations. We compute the dark matter capture rate as a function of the dark matter mass and scattering cross section using the formulae from [52] and assuming a local WIMP density of 0.3 GeV/cm^3 with an isothermal velocity distribution and velocity dispersion 220 km/sec. We assume the annihilation cross section to be large enough for the capture and annihilation reactions to be in equilibrium,
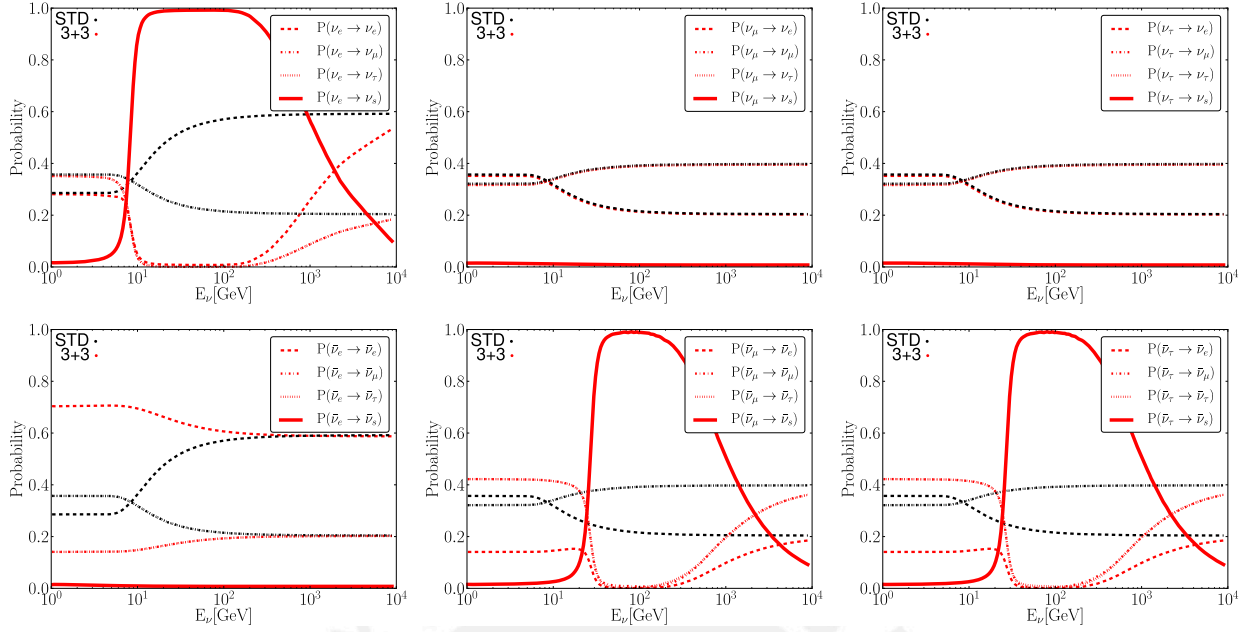
Figure 2: Flavor transition probabilities in the Sun as a function of energy for an initial ν_e (left), an initial ν_μ (center), and an initial ν_τ (right). The top plots are for neutrinos, the ones at the bottom are for anti-neutrinos. Black lines are for standard three-flavor oscillation, whereas red lines are for a "$3+3$" toy model with three sterile neutrinos (see text for details). Absorption and τ regeneration effects are neglected in these plots. Note that the black dotted lines ($\nu_x \to \nu_\tau$ in the SM) and the black dot-dashed lines ($\nu_x \to \nu_\mu$ in the SM) lie on top of each other since ν_μ–ν_τ mixing is assumed to be maximal.
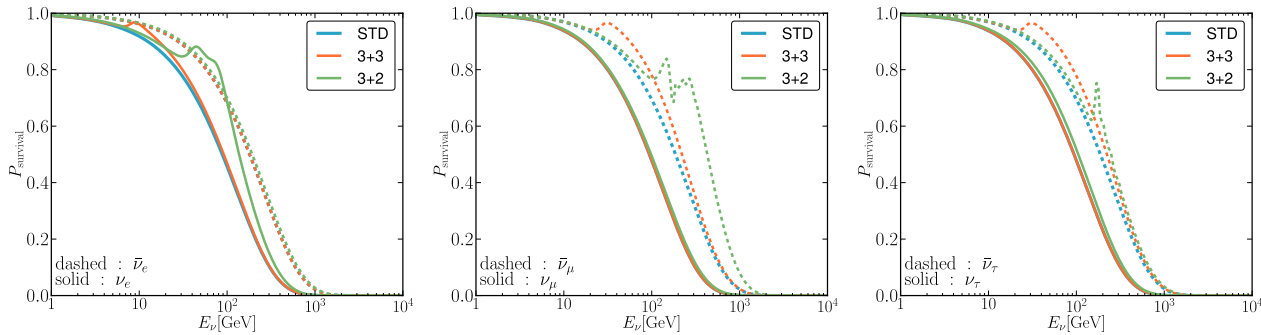

Figure 3: Survival (= non-interaction) probabilities for high-energy neutrinos from dark matter annihilation on their way out of the Sun. We show results for standard three-flavor oscillations, for the best fitting $3+2$ model, and for a $3+3$ toy model. The features in the $3+2$ and $3+3$ curves are due to the interplay of active–sterile conversion and active neutrino interactions.

so that the annihilation rate is equal to half the capture rate. We use initial neutrino spectra from [53], which were generated using `WimpSim` [54].

To propagate the neutrinos out of the Sun, we use our own Monte Carlo code, which is capable of working with an arbitrary number of neutrino flavors n, and simulates n-flavor oscillations in matter as well as NC and CC neutrino scattering in the Sun, including τ regeneration. We use the `nusigma` package [53, 54] to calculate the neutrino cross sections, and TAUOLA [55] for decaying

secondary τ's.

In practice, we proceed as follows: We propagate the n-component neutrino state vector $\psi(t)$ out of the Sun using the `rkf45` Runge-Kutta-Fehlberg algorithm from the GNU Scientific Library [56] to solve the evolution equation

$$
i\frac{d}{dt}\psi(t) = \frac{1}{2E}U\begin{pmatrix} 0 & & & & \\ & \Delta m_{21}^2 & & & \\ & & \Delta m_{31}^2 & & \\ & & & \Delta m_{41}^2 & \\ & & & & \ddots \end{pmatrix}U^\dagger\psi(t) + \sqrt{2}G_F\begin{pmatrix} N_e(t) - \frac{N_n(t)}{2} & & & & \\ & -\frac{N_n(t)}{2} & & & \\ & & -\frac{N_n(t)}{2} & & \\ & & & 0 & \\ & & & & \ddots \end{pmatrix}\psi(t).
$$

(12)

After each Runge-Kutta step, we determine randomly if the neutrino undergoes an incoherent interactions during that step. The probability for a CC or NC interaction is given by $P_{\mathrm{CC/NC}} = \sigma_{\mathrm{CC/NC}}/(\sigma_{\mathrm{CC}} + \sigma_{\mathrm{NC}}) \times \left[1 - \exp\left(-\Delta r\, n(r)\,(\sigma_{\mathrm{CC}} + \sigma_{\mathrm{NC}})\right)\right]$, where $n(r)$ is the local nucleon number density, $\sigma_{\mathrm{CC(NC)}}$ is the charged current (neutral current) neutrino–nucleon scattering cross section, and Δr is the current Runge-Kutta step size. If it is determined that the neutrino interacts through a neutral current, its energy after the interaction is picked randomly from the final state energy spectrum calculated using `nusigma` [53, 54]. Since we are treating neutrino propagation as a one-dimensional problem, we assume that the direction of travel does not change, and we continue to propagate the neutrino radially outward. In the case of a ν_e or ν_μ charged current interactions, we simply discard the neutrino. In a charged current ν_τ interactions, the original neutrino is also absorbed, but since the secondary τ lepton (unlike a secondary muon from a ν_μ interaction) decays before it is stopped in matter, new high-energy neutrinos can be produced from its decay ("τ regeneration"). We use `TAUOLA` [55] to simulate τ decay, and propagate all secondary high-energy neutrinos out of the Sun individually.

We compute the expected event rate in the IceCube detector by multiplying the differential muon neutrino and antineutrino fluxes at the Earth the effective detector area $A_{\mathrm{eff}}(E)$ [57] and then integrating over energy. We have checked that Earth shadowing effects [58, 59] are negligible for our results. Note that the effective area given in [57] has been computed from a simulation of the full 86-string IceCube detector, whereas the latest published dark matter limits from IceCube are based on data taken in the 40-string IceCube configuration and in the older AMANDA-II detector. Since we will ultimately use our simulation only to compute *ratios* of event rates between different oscillation models, we expect the systematic bias introduced that way to be small. Note also that $A_{\mathrm{eff}}(E)$ as given in [57] is the combined effective area for neutrinos and antineutrinos. Since in sterile neutrino models, the relative importance of neutrinos and antineutrinos in the IceCube signal changes, we need seperate effective areas for neutrinos ($A_{\mathrm{eff}}^\nu(E)$) and antineutrinos ($A_{\mathrm{eff}}^{\bar\nu}(E)$). We obtain them according to

$$
A_{\mathrm{eff}}^\nu(E) = A_{\mathrm{eff}}(E)\frac{\sigma_{\mathrm{CC}}^\nu(E)\,d_{\mu^-}(E_\mu)}{\sigma_{\mathrm{CC}}^\nu(E)\,d_{\mu^-}(E_\mu) + \sigma_{\mathrm{CC}}^{\bar\nu}(E)\,d_{\mu^+}(E_\mu)}\,,
$$

(13)

$$
A_{\mathrm{eff}}^{\bar\nu}(E) = A_{\mathrm{eff}}(E)\frac{\sigma_{\mathrm{CC}}^\nu(E)\,d_{\mu^-}(E_\mu)}{\sigma_{\mathrm{CC}}^\nu(E)\,d_{\mu^-}(E_\mu) + \sigma_{\mathrm{CC}}^{\bar\nu}(E)\,d_{\mu^+}(E_\mu)}\,,
$$

(14)

with the charged current neutrino–nucleon (antineutrino–nucleon) cross section $\sigma_{\mathrm{CC}}^\nu(E)$ ($\sigma_{\mathrm{CC}}^{\bar\nu}(E)$), and the muon (antimuon) range $d_{\mu^-}(E_\mu)$ ($d_{\mu^+}(E_\mu)$). For simplicity, we assume a one-to-one relation between the neutrino energy E and the secondary muon energy E_μ: $E_\mu = (1 - y_{\mathrm{CC}}(E_\nu))E_\nu$, where y_{CC} is the mean charged current inelasticity parameter [60]. We have checked that using full differential cross sections would not significantly change our results.
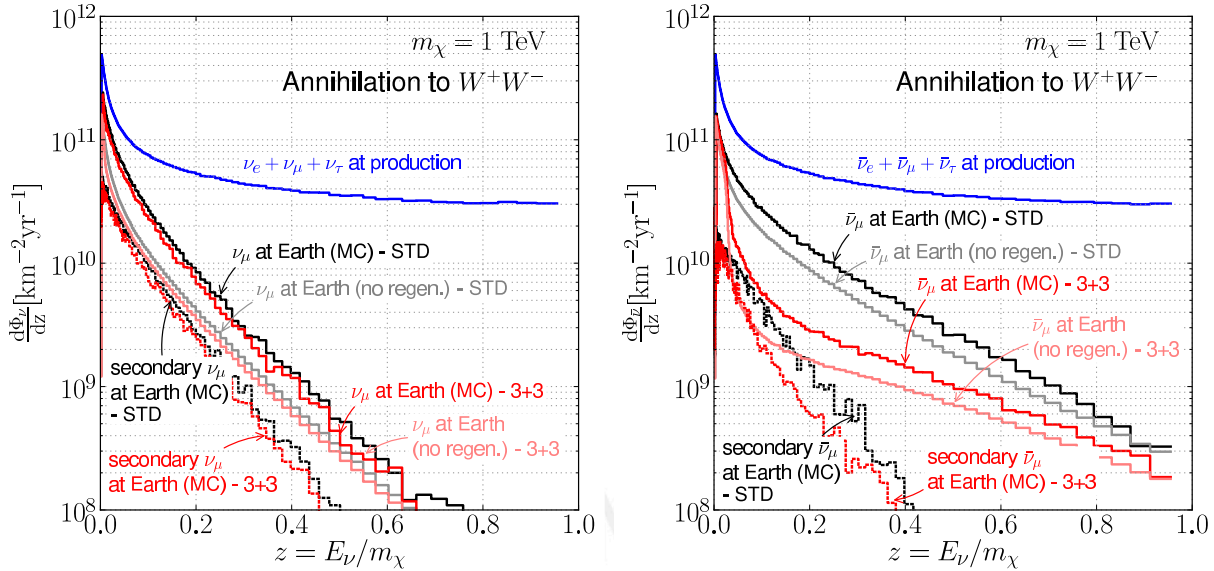
Figure 4: Predicted neutrino fluxes (left) and antineutrino fluxes (right) for annihilation of a 1 TeV WIMP into W^+W^- in the Sun. We show the total neutrino flux at production, as well as the muon neutrino flux at the Earth. For illustration, we also show the flux of secondary neutrinos from τ regeneration, as well as the flux obtained using the simplified calculation that neglects regeneration and partial energy loss (see text for details). Results for standard oscillations are shown in black, results for the $3+3$ toy model introduced in section II are shown in red.

We have verified our Monte Carlo code by comparing its predictions to published results from [53, 54, 61, 62].

While the advantage of the Monte Carlo technique is certainly its flexibility, it is also quite computationally intensive. Since we are also interested in carrying out parameter scans over different sets of sterile neutrino parameters (see section V below), we have also developed a faster code, which does not take into account τ regeneration and energy loss in neutral current interactions. Instead, it simply considers all neutrinos that interact in the Sun in any way (NC or CC) to be lost to detection. Thus, for each given set of oscillation parameters and for each neutrino energy, we need to solve the equation of motion only once to determine the oscillation probabilities for those neutrinos which do not interact. At each Runge-Kutta step, we also keep track of the interaction probability to obtain simultaneously the fraction of neutrinos at the considered energy which leave the Sun without interacting.

We compare the results of our full Monte Carlo simulation to those of the simplified method in figure 4. We also show the flux of secondary neutrinos from τ regeneration, and we notice that these neutrinos account for most of the difference between the MC results and the ones from the simplified method. (Another small contribution to this difference comes from neutrinos that have undergone NC scattering, but are still within the accessible energy range.) This conclusion is the same for standard three-flavor oscillations (black and gray curves in figure 4) and for the $3+3$ model (red curves).

IV. MODIFIED ICECUBE LIMITS ON DARK MATTER CAPTURE IN THE SUN

In figure 5 we show how the IceCube limits on spin-dependent dark matter–proton scattering need to be modified if sterile neutrinos exist (black and gray lines). For comparison we also show as colored lines limits from a number of direct dark matter searches. Solid black lines in figure 5 are the published IceCube limits from [27, 57]; Dashed and dotted lines show the constraint obtained in the $3 + 2$ model and the $3 + 3$ toy model introduced in section II, respectively. To obtain these results, we have used the methods described in section III to predict the ratio of the event rates at IceCube with and without sterile neutrinos, and we have then rescaled the published IceCube 90% CL limit on the dark matter–nucleon scattering cross section $\sigma_{90,\text{STD}}$ (which was computed assuming standard oscillations) by this ratio. Specifically, if we denote the IceCube event rate by N_{STD}, N_{3+2} and N_{3+3} for the standard oscillation, $3 + 2$, and $3 + 3$ scenarios, respectively, we compute the cross section limits in the $3 + 2$ and $3 + 3$ scenarios, $\sigma_{90,3+2}$ and $\sigma_{90,3+3}$, according to

$$\sigma_{90,3+2} = \sigma_{90,\text{STD}} \frac{N_{3+2}}{N_{\text{STD}}}, \tag{15}$$

$$\sigma_{90,3+3} = \sigma_{90,\text{STD}} \frac{N_{3+3}}{N_{\text{STD}}}. \tag{16}$$

We see that the $3 + 2$ model leads to a moderate weakening of the cross section limit, which can be understood from the fact that only electron neutrinos ν_e and muon antineutrinos $\bar{\nu}_\mu$ are substantially transformed into sterile states (see figure 1), and that these transitions happen only for neutrinos with energies above several hundred GeV, whose contribution to the muon flux at IceCube is suppressed due to the large absorption probability in the Sun. In the $3 + 3$ toy model, on the other hand, resonant flavor transitions happen already at lower energy (see figure 2), and they happen for ν_e, $\bar{\nu}_\mu$ and $\bar{\nu}_\tau$.

As mentioned in section II, the effect could be even stronger if Δm_{41}^2, Δm_{51}^2, and Δm_{61}^2 were negative (which might, however, require non-standard cosmology to be consistent).

V. DEPENDENCE ON STERILE NEUTRINO PARAMETERS

In section IV we have illustrated using two exemplary models how neutrino limits on dark matter capture and annihilation in the Sun are modified by oscillations into sterile neutrinos . We are now going to study more systematically how the worsening of these limits depends on the sterile neutrino parameters. We do this using the $3+3$ toy model introduced in section II since this model has only two new parameters (θ_s and Δm_s^2), but still covers the most important phenomenological aspects of more general sterile neutrino scenarios.

We show in figure 6 the factor by which the IceCube limits on the spin-dependent dark matter–nucleon scattering cross section are weakened for a wide range of $\sin^2 2\theta_s$ and Δm_s^2 values. The shape of the contours can be understood as follows: At very large Δm_s^2, the new MSW resonances, equations (9)–(11) lie at a very high neutrino energy. For instance, at $\Delta m_s^2 = 1$ eV^2, equation (9) yields a resonance energy of about 60 GeV at solar core densities, i.e. only neutrinos with $E \gtrsim 60$ GeV are affected by the resonance. Since very high energy neutrinos are mostly absorbed in the Sun, they do not contribute significantly to the IceCube limits. For somewhat lower Δm_s^2, the resonances move down in energy into the region relevant to IceCube. For too low Δm_s^2 or for too small θ_s, on the other hand, MSW-enhanced flavor transitions become non-adiabatic (see equation (3) and related discussion), suppressing active–sterile transitions again. This happens first at high energy, which is why at low Δm_s^2 the correction factors shown in figure 6 are generally larger for dark matter annihilation into the soft $\bar{b}b$ channel than for annihilation in to the hard W^+W^- final state.
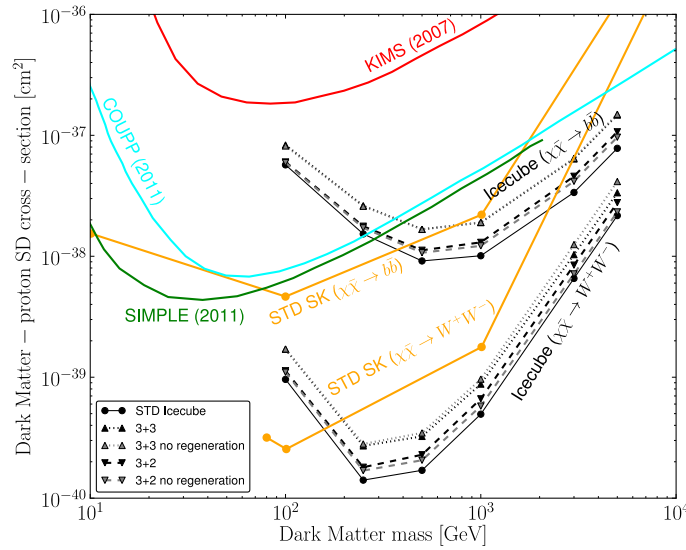
Figure 5: IceCube limits on spin-dependent dark matter-proton scattering [27, 57] in scenarios with (black/gray dashed and dotted lines) and without (black/gray solid lines) sterile neutrinos compared to data from direct detection experiments [24, 63–65] and from Super-Kamiokande (SK) [25] (colored lines). Black lines correspond to results based on our Monte Carlo (MC) code, whereas gray lines are based on a simplified calculation which does not include secondary neutrinos (see text for details). We see that for the $3+2$ scenario which provides the best fit to short baseline neutrino oscillation data, the limits are only moderately weakened. Our $3+3$ toy model, on the other hand, illustrates that larger modifications are possible.

VI.   DISCUSSION AND CONCLUSIONS

In this paper, we have shown how IceCube limits on dark matter capture and annihilation in the Sun are modified if eV-scale sterile neutrinos exist, as suggested by part of the short baseline oscillation data. Since IceCube is looking for high-energy neutrinos from dark matter annihilation in the center of the Sun, its results depend strongly on the oscillations of these neutrinos on their way out of the Sun. We have argued that in sterile neutrino scenarios new high-energy MSW resonances can lead to almost complete conversion of certain neutrino flavors into sterile states inside the Sun. In this case IceCube's constraints on dark matter–nucleon scattering can be significantly weakened, by a factor of two or more.

This may have interesting implications if in the future dark matter is detected in a direct search or at the LHC, but the parameters determined there are in conflict with limits (or signals) from neutrino telescopes. If the allowed dark matter annihilation channels and branching fractions are established at the LHC, such a conflict could then provide a clear and strong hint for the existence of sterile neutrinos. With sufficient data, neutrino telescopes would even be able to contribute the determination of the active–sterile mixing parameters.

Note added: While we were completing this work, reference [66] appeared on the arXiv, addressing similar topics.
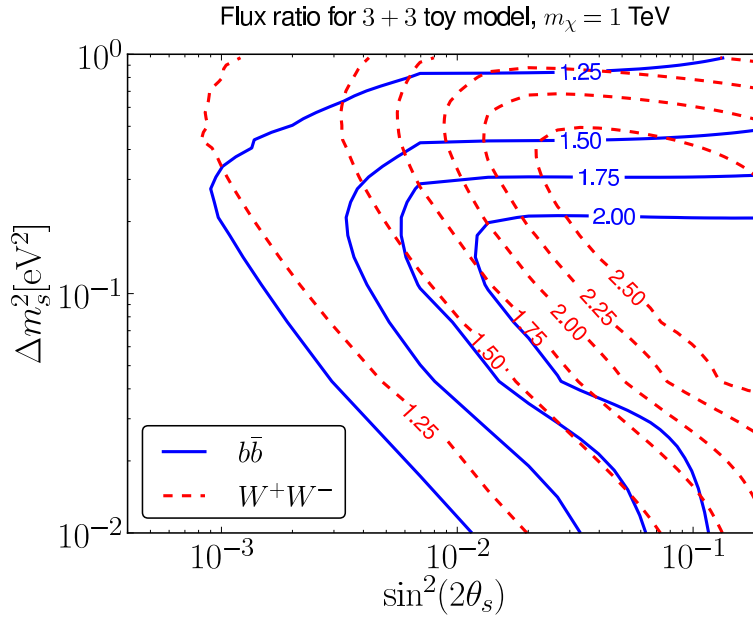
Figure 6: Weakening of IceCube limits on dark matter capture and annihilation in the Sun due to sterile neutrinos, assuming for illustrative purposes the $3+3$ toy model introduced in section II. The contours show the factor by which the IceCube limit on spin-dependent dark matter–proton scattering cross section for a 1 TeV WIMP. Red dashed contours are for annihilation into W^+W^- (which yields a rather hard neutrino spectrum), blue solid contours are for annihilation into $\bar{b}b$ (which yields a much softer spectrum). At large Δm_s^2, oscillations into sterile neutrinos become less relevant because the active–sterile MSW resonances move to very high energies; at small Δm_s^2 or small $\sin^2 2\theta_s$, the MSW transitions become non-adiabatic.

Acknowledgments

It is a pleasure to thank Matthias Danninger for very useful discussions on the IceCube dark matter search. We are also grateful to the Dirección de Informática Académica at the Pontificia Universidad Católica del Perú (PUCP) for providing distributed computing support through the LEGION system. CA would like to thank Fermilab for warm hospitality and for support through the Latin American Students Program during his six month visit in summer 2011. CA is supported by the Dirección de Gestión de la Investigación at PUCP through grant DGI-2011-0180. Fermilab is operated by Fermi Research Alliance, LLC, under contract DE-AC02-07CH11359 with the United States Department of Energy.

Appendix A: Numerics of neutrino oscillation probabilities

In this appendix, we discuss the algorithm used to compute the neutrino oscillation probabilities in the Sun. As mentioned in section III we use an implementation of the well known Runge-Kutta (RK) algorithm [67], namely the `rkf45` algorithm implemented in the GNU Scientific Library [56]. In each iteration this algorithm uses a step function to evolve the neutrino state vector from a time t_0 to a time $t_0 + \Delta t$ by approximately solving the Schrödinger equation, where Δt is chosen such that the optimal balance between speed and accuracy is achieved. Rather than working entirely in one basis, we transform the Schrödinger equation to an instantaneous interaction basis before

each step. This instantaneous interaction basis is defined by the transformation

$$\psi_I(t; t_0) = S(t, t_0)\, \psi(t) \equiv e^{iH_0(t-t_0)} \psi(t)\,, \tag{A1}$$

where the Hamiltonian has been separated in the following manner

$$H(t) = H(t_0) + \Delta H(t; t_0)\,, \tag{A2}$$

with

$$H_0(t_0) = \frac{1}{2E} U D U^\dagger + V(t_0)\,, \qquad \Delta H(t; t_0) = V(t) - V(t_0)\,. \tag{A3}$$

Here $V(t)$ is the neutrino matter potential (see equation (4)), E the neutrino energy, U the leptonic mixing matrix, and $D = \mathrm{diag}(0, \Delta m_{21}^2, \Delta m_{31}^2, ...)$.

The Schrödinger equation in the interaction basis is

$$i\frac{d\psi_I}{dt} = H_I \psi_I \tag{A4}$$

with $H_I(t; t_0) = S(t, t_0)\, \Delta H\, S^\dagger(t, t_0)$. Since the matter potential changes slowly in the Sun and thus H_I is small, the RK algorithm can choose a larger step size Δt compared to a calculation in the flavor basis. Note that the elements S_{jk} of the transformation matrix $S(t, t_0)$ can be evaluated efficiently by computing $\tilde{V}_{jm} e^{-i\lambda_m(t-t_0)} (\tilde{V}^\dagger)_{mk}$, where λ_m are the eigenvalues of H_0, and $\tilde{V}$ is the matrix of the corresponding eigenvectors. After the evolution of the step has concluded we transform ψ_I back to the flavor basis,

$$\psi(t_0 + \Delta t) = e^{-iH_0(t_0)\,\Delta t} \psi_I(t_0 + \Delta t)\,, \tag{A5}$$

and proceed to the next step, setting $t_0 \to t_0 + \Delta t$.

[1] C. Aalseth *et al.* (CoGeNT collaboration), Phys.Rev.Lett., **106**, 131301 (2011), arXiv:1002.4703 [astro-ph.CO] .

[2] C. Aalseth, P. Barbeau, J. Colaresi, J. Collar, J. Leon, *et al.*, (2011), arXiv:1106.0650 [astro-ph.CO] .

[3] R. Bernabei *et al.* (DAMA), Eur. Phys. J., **C56**, 333 (2008), arXiv:0804.2741 [astro-ph] .

[4] R. Bernabei, P. Belli, F. Cappella, R. Cerulli, C. Dai, *et al.*, Eur.Phys.J., **C67**, 39 (2010), arXiv:arXiv:1002.1028 [astro-ph.GA] .

[5] G. Angloher, M. Bauer, I. Bavykina, A. Bento, C. Bucci, *et al.*, (2011), arXiv:1109.0702 [astro-ph.CO] .

[6] Z. Ahmed *et al.* (The CDMS-II Collaboration), Science, **327**, 1619 (2010), arXiv:0912.3592 [astro-ph.CO] .

[7] Z. Ahmed *et al.* (CDMS-II Collaboration), Phys.Rev.Lett., **106**, 131302 (2011), arXiv:1011.2482 [astro-ph.CO] .

[8] E. Aprile *et al.* (XENON100 Collaboration), Phys.Rev.Lett. (2011), arXiv:1104.2549 [astro-ph.CO] .

[9] J. Collar, (2011), arXiv:1103.3481 [astro-ph.CO] .

[10] J. Collar, (2011), arXiv:1106.0653 [astro-ph.CO] .

[11] M. T. Frandsen, F. Kahlhoefer, J. March-Russell, C. McCabe, M. McCullough, *et al.*, (2011), arXiv:1105.3734 [hep-ph] .

[12] P. J. Fox, J. Kopp, M. Lisanti, and N. Weiner, (2011), arXiv:1107.0717 [hep-ph] .

[13] M. Farina, D. Pappadopulo, A. Strumia, and T. Volansky, (2011), arXiv:1107.0715 [hep-ph] .

[14] T. Schwetz and J. Zupan, (2011), arXiv:1106.6241 [hep-ph] .

[15] C. McCabe, (2011), arXiv:1107.0741 [hep-ph] .

[16] J. Kopp, T. Schwetz, and J. Zupan, (2011), arXiv:1110.2721 [hep-ph] .

[17] D. Hooper and C. Kelso, (2011), arXiv:1106.1066 [hep-ph] .

[18] P. Belli, R. Bernabei, A. Bottino, F. Cappella, R. Cerulli, *et al.*, (2011), arXiv:1106.4667 [hep-ph] .

[19] C. Kelso, D. Hooper, and M. R. Buckley, (2011), arXiv:1110.5338 [astro-ph.CO] .

[20] M. T. Frandsen, F. Kahlhoefer, C. McCabe, S. Sarkar, and K. Schmidt-Hoberg, (2011), arXiv:1111.0292 [hep-ph] .

[21] O. Adriani *et al.* (PAMELA Collaboration), Nature, **458**, 607 (2009), arXiv:0810.4995 [astro-ph] .

[22] A. A. Abdo *et al.* (The Fermi LAT Collaboration), Phys.Rev.Lett., **102**, 181101 (2009), arXiv:0905.0025 [astro-ph.HE] .

[23] L. Bergstrom, J. Edsjo, and G. Zaharijas, Phys.Rev.Lett., **103**, 031103 (2009), arXiv:0905.0333 [astro-ph.HE] .

[24] S. Desai *et al.* (Super-Kamiokande), Phys. Rev., **D70**, 083523 (2004), arXiv:hep-ex/0404025 .

[25] T. Tanaka *et al.* (Super-Kamiokande Collaboration), Astrophys.J., **742**, 78 (2011), long author list - awaiting processing, arXiv:1108.3384 [astro-ph.HE] .

[26] R. Abbasi *et al.* (ICECUBE), Phys. Rev. Lett., **102**, 201302 (2009), arXiv:0902.2460 [astro-ph.CO] .

[27] I. Collaboration (IceCube Collaboration), (2011), arXiv:1112.1840 [astro-ph.HE] .

[28] A. Aguilar *et al.* (LSND), Phys. Rev., **D64**, 112007 (2001), hep-ex/0104049 .

[29] A. A. Aguilar-Arevalo *et al.* (MiniBooNE), Phys. Rev. Lett., **105**, 181801 (2010), arXiv:1007.1150 [hep-ex] .

[30] T. Mueller, D. Lhuillier, M. Fallot, A. Letourneau, S. Cormon, *et al.*, Phys.Rev., **C83**, 054615 (2011), arXiv:1101.2663 [hep-ex] .

[31] G. Mention, M. Fechner, T. Lasserre, T. Mueller, D. Lhuillier, *et al.*, Phys.Rev., **D83**, 073006 (2011), arXiv:1101.2755 [hep-ex] .

[32] P. Huber, (2011), arXiv:1106.0687 [hep-ph] .

[33] J. Kopp, M. Maltoni, and T. Schwetz, (2011), arXiv:1103.4570 [hep-ph] .

[34] C. Giunti and M. Laveder, (2011), arXiv:1107.1452 [hep-ph] .

[35] C. Giunti and M. Laveder, (2011), arXiv:1109.4033 [hep-ph] .

[36] S. Razzaque and A. Smirnov, JHEP, **1107**, 084 (2011), arXiv:1104.1390 [hep-ph] .

[37] V. Barger, Y. Gao, and D. Marfatia, (2011), arXiv:1109.5748 [hep-ph] .

[38] J. N. Bahcall, A. M. Serenelli, and S. Basu, Astrophys.J., **621**, L85 (2005), Solar model data available from http://www.sns.ias.edu/~jnb/, arXiv:astro-ph/0412440 [astro-ph] .

[39] S. P. Mikheyev and A. Y. Smirnov, Sov. J. Nucl. Phys., **42**, 913 (1985).

[40] S. P. Mikheyev and A. Y. Smirnov, Nuovo Cim., **C9**, 17 (1986).

[41] L. Wolfenstein, Phys. Rev., **D17**, 2369 (1978).

[42] E. K. Akhmedov, (1999), hep-ph/0001264 .

[43] T. Schwetz, M. Tortola, and J. Valle, New J.Phys., **13**, 109401 (2011), arXiv:1108.1376 [hep-ph] .

[44] T. Schwetz, M. Tortola, and J. Valle, New J.Phys., **13**, 063004 (2011), arXiv:1103.0734 [hep-ph] .

[45] A. E. Nelson and J. Walsh, Phys.Rev., **D77**, 033001 (2008), arXiv:arXiv:0711.1363 [hep-ph] .

[46] J. Hamann, S. Hannestad, G. G. Raffelt, I. Tamborra, and Y. Y. Wong, Phys.Rev.Lett., **105**, 181301 (2010), arXiv:1006.5276 [hep-ph] .

[47] E. Giusarma, M. Corsi, M. Archidiacono, R. de Putter, A. Melchiorri, *et al.*, Phys.Rev., **D83**, 115023 (2011), arXiv:1102.4774 [astro-ph.CO] .

[48] J. Hamann, S. Hannestad, G. G. Raffelt, and Y. Y. Wong, JCAP, **1109**, 034 (2011), arXiv:1108.4136 [astro-ph.CO] .

[49] E. Giusarma, M. Archidiacono, R. de Putter, A. Melchiorri, and O. Mena, (2011), arXiv:1112.4661 [astro-ph.CO] .

[50] G. Gelmini, S. Palomares-Ruiz, and S. Pascoli, Phys.Rev.Lett., **93**, 081302 (2004), arXiv:astro-ph/0403323 [astro-ph] .

[51] A. Y. Smirnov and R. Zukanovich Funchal, Phys.Rev., **D74**, 013001 (2006), arXiv:hep-ph/0603009 [hep-ph] .

[52] A. Gould, Astrophys. J. , **388**, 338 (1992).

[53] M. Blennow, J. Edsjo, and T. Ohlsson, (2007), http://www.physto.se/~edsjo/wimpsim/.

[54] M. Blennow, J. Edsjo, and T. Ohlsson, JCAP, **0801**, 021 (2008), arXiv:0709.3898 [hep-ph] .

[55] S. Jadach, Z. Was, R. Decker, and J. H. Kuhn, Comput.Phys.Commun., **76**, 361 (1993).

[56] M. Galassi *et al.*, *GNU Scientific Library Reference Manual*, 2nd ed. (Network Theory Ltd., 2003) ISBN 0-9541-617-34, http://www.gnu.org/software/gsl/.

[57] The IceCube Collaboration, (2011), arXiv:1111.2738 [astro-ph.HE] .

[58] C. Arguelles, M. Bustamante, and A. Gago, JCAP, **1012**, 005 (2010), arXiv:1008.1396 [astro-ph.HE] .

[59] H. B. Koers and P. Tinyakov, Phys.Rev., **D78**, 083009 (2008), arXiv:0802.2403 [astro-ph] .

[60] R. Gandhi, C. Quigg, M. H. Reno, and I. Sarcevic, Phys.Rev., **D58**, 093009 (1998), arXiv:hep-ph/9807264 [hep-ph] .

[61] M. Cirelli *et al.*, Nucl. Phys., **B727**, 99 (2005), arXiv:hep-ph/0506298 .

[62] C. Giunti and Y. Li, Phys.Rev., **D80**, 113007 (2009), arXiv:0910.5856 [hep-ph] .

[63] H. S. Lee *et al.* (KIMS), Phys. Rev. Lett., **99**, 091301 (2007), arXiv:0704.0423 [astro-ph] .

[64] E. Behnke, J. Behnke, S. Brice, D. Broemmelsiek, J. Collar, *et al.*, Phys.Rev.Lett., **106**, 021303 (2011), the updated results reproduced here were presented at TAUPP 2011, see http://taup2011.mpp.mpg.de/, arXiv:1008.3518 [astro-ph.CO] .

[65] M. Felizardo, T. Girard, T. Morlat, A. Fernandes, F. Giuliani, *et al.*, (2011), * Temporary entry *, arXiv:1106.3014 [astro-ph.CO] .

[66] A. Esmaili and O. L. Peres, (2012), arXiv:1202.2869 [hep-ph] .

[67] J. Stoer *et al.*, *Introduction to Numerical Analysis*, 3rd ed. (Springer, 2002) ISBN 038795452X.